Decoding the oxygen isotope signal for seasonal growth patterns in Arctic bivalves

Vihtakari Mikko[1,2,3,*], Renaud Paul E.[3,4], Clarke Leon J.[5], Whitehouse Martin J.[6], Hop Haakon[2], Carroll Michael L.[3], Ambrose Jr. William G.[3,7]

1 Department of Arctic and Marine Biology, UiT The Arctic University of Norway, N-9037 Tromsø, Norway
2 Norwegian Polar Institute, Fram Centre, N-9296 Tromsø, Norway
3 Akvaplan-niva, Fram Centre, N-9296 Tromsø, Norway
4 University Centre in Svalbard, N-9171 Longyearbyen, Norway
5 School of Science and the Environment, Faculty of Science and Engineering, Manchester Metropolitan University, Manchester, M1 5GD, UK
6 Department of Geosciences, Swedish Museum of Natural History, SE-10405 Stockholm, Sweden
7 Department of Biology, Bates College, Lewiston, Maine 04240, USA
∗ E-mail: mikko.vihtakari@gmail.com

Keywords: *Serripes groenlandicus*; *Ciliatocardium ciliatum*; *in situ* δ^{18}O analyses; Secondary ion mass spectrometry; R package development; Dynamic time warping; sclerochronology

Abstract

Chemical and physical variation in skeletal structures of marine organisms can reflect environmental variability, forming the basis for reconstructing the conditions in which the organism lived. The successful use of these bio-archives for reconstructing seasonal and sub-seasonal environmental conditions is dependent on understanding sub-annual growth patterns and the timing of deposition of visible markers. We studied sub-annual shell growth patterns, as well as the timing and environmental processes initiating winter growth line deposition in two circumpolar bivalve mollusks, *Serripes groenlandicus* and *Ciliatocardium ciliatum*. Shell growth deposited during a 1-year deployment on oceanographic moorings in Kongsfjorden and Rijpfjorden, Svalbard, was analyzed *in situ* for δ^{18}O using high spatial resolution secondary ion mass spectrometry (SIMS). A new digital method was developed to measure the location of SIMS spots along chronologically deposited shell material. Dynamic time warping (DTW) algorithms were adapted to align SIMS-determined δ^{18}O values with δ^{18}O values predicted from continuous mooring instrument recordings of seawater temperature and salinity, in order to derive sub-annual shell growth models. The resulting growth models indicated that the prominent winter growth band was formed during a slow shell growth period lasting from December until May in Kongsfjorden and from November until mid-June in Rijpfjorden. The length of the slow growth period during winter was most likely controlled by food availability. Shell growth rate during the growing season was significantly explained by temperature (marginal $R^2 = 0.29$) indicating that temperature is a major driver of shell growth rate when the food supply is sufficient. The insights of sub-annual growth of Arctic bivalves and the methods developed in our study are important contributions for further development of bivalve shells as proxy archives.

Introduction

Detailed records of oceanic conditions across a range of spatial and temporal scales are needed to understand implications of the rapid climate change on sensitive ecosystems [1]. This is especially true for the Arctic Ocean, where instrumental records are sparse [2] and the climate change is projected to be most pronounced [3–6]. Skeletal structures of calcifying marine organisms provide archives of ocean conditions that can be interpreted based on the geochemical signatures preserved within the calcium carbonate ($CaCO_3$) deposited during the life-time of the animal [7–11]. Visible growth lines deposited within these skeletal structures can be used as time markers to reconstruct their growth patterns back through time [12–15]. Marine organisms do not have a constant growth rate through time, complicating the dating of geochemical samples from their hard parts [15, 16]. Knowledge of species-specific growth patterns and their seasonality is therefore required in order to facilitate interpretation of sub-annual geochemical proxy records [14].

High-latitude bivalve mollusks, such as *Serripes groenlandicus* Mohr, 1786 and *Ciliatocardium ciliatum* Fabricius, 1780, are long lived filter-feeding organisms that record ocean conditions within their aragonitic shells [17–19]. Their shell growth is sensitive to changes in food supply and temperature [15, 20], and is regulated by large scale climatic drivers over annual to decadal scales [21–24]. Both species deposit prominent annual growth lines during winter that can be used to construct decadal to multi-centennial chronologies, with the possibility of sampling geochemical information on sub-seasonal resolution [10, 14, 15, 25, 26]. The usage of geochemical signatures, such as element-to-calcium ratios [18], as sub-annual proxies of seawater conditions has been difficult in these species, because the processes that trigger the deposition of the annual growth lines or the months during which these growth lines form are unknown [15]. Sejr *et al.* [20] suggested that shell growth of *C. ciliatum* is controlled by food availability due to significant negative correlations between annual sea-ice cover and shell increment width. The authors were, however, unable to further quantify this relationship due to lack of data on food availability and sub-seasonal growth rates. Furthermore, Ambrose *et al.* [15] suggested that a shortage of food triggers the deposition of the winter growth lines in *S. groenlandicus* and *C. ciliatum*, but the lack of sub-annual shell growth models prevented testing of that hypothesis and precluded estimating dates when the winter growth line was deposited. Identifying the specific timing of seasonal growth line deposition and the development of sub-annual shell growth models are necessary first steps for further geochemical proxy studies using these species.

The ratio of stable oxygen isotopes ($^{18}O/^{16}O$, denoted as $\delta^{18}O_{VPDB}$ values, expressed in parts per thousand relative to the Vienna PeeDee belemnite international reference) in biogenic carbonates, such as *S. groenlandicus* shells [25], is a well established geochemical proxy that can be used to reconstruct seawater temperatures, when the oxygen-isotope composition of the water ($\delta^{18}O_w$) is known [27–29]. If seawater salinity, temperature, and a salinity–$\delta^{18}O_w$ relationship [30] are known, these variables can be used to calculate the expected $\delta^{18}O$ values in bivalve shell $CaCO_3$ [31], thereby enabling determination of bivalve shell growth patterns [14, 32, 33].

Oxygen-isotope ratio analyses on bivalve mollusk shells are conventionally implemented by milling $CaCO_3$ powder along sectioned shells [18, 32, 34, 35]. Carbon dioxide acquired by phosphoric acid digestion of sampled $CaCO_3$ powder is then analyzed for $\delta^{18}O$ values using a gas-source isotope ratio mass spectrometer with a typical precision of c. 0.05 ‰ [36]. However, this conventional method, requires relatively large sample sizes (> 10 µg), leading to a spatial

resolution of sampling that is incapable of investigating sub-annual growth banding of Arctic bivalves with a slow growth rate (few mm y^{-1}). In contrast, surface (= *in situ*) $\delta^{18}O$ analysis by secondary ion mass spectrometry (SIMS), with a typical probe diameter of c. 10 μm and limited depth penetration (< 2 μm), consumes a much smaller amount of sample (c. 0.5 ng) compared to the conventional analysis. SIMS analysis is preferred when high spatial resolution sampling is required [e.g. 37], as long as the expected variation in $\delta^{18}O$ values exceeds the lower precision obtained by the method (ca. 0.2 ‰).

A notable drawback of SIMS analysis of $\delta^{18}O$, however, is that it sputters oxygen from all phases within the sampled volume, including organic-hosted oxygen [38] and carbonate-hosted sulphate [38, 39]. Further, SIMS-determined $\delta^{18}O$ values are depleted in the heavy isotopes compared to the true isotopic abundances, because light ions are more easily emitted during the sputtering process relative to heavy ions due to the differences in energy of ions with different masses and bond energy discrepancies among sputtered molecules [37, 40]. Although this effect, called instrumental mass fractionation (IMF), is accounted for by usage of reference materials, the magnitude of IMF is reported to vary among $CaCO_3$ minerals, such as calcite and aragonite [37, 41, 42]. Consequently, the $\delta^{18}O$ values acquired by SIMS can differ from values obtained using the conventional phosphoric acid digestion method [31, 43, 44], and thus from predictions generated for the latter.

Spot samples taken along a section of chronologically deposited shell material generate two issues that complicate the interpretation of the measured geochemical signals. First, sample spot location is difficult to determine using distance from a defined position, such as the shell margin, if the sample spots are not aligned along a sequence consistently perpendicular to growth lines. Some studies on bivalve mollusk shells overcame this issue by sampling at locations where the sampling sequence can be placed perpendicularly against the growth lines, such as the umbo region [e.g. 45, 46]. This practice, however, limits the sampling resolution since most shell growth occurs at the shell margin. Second, time averaging of sample material is, in principle, always present when shell material is physically sampled, thereby leading to a systematic underestimation of peaks and troughs in geochemical signals [47, 48]. The magnitude of this phenomenon, also referred to as "time-averaging error", depends on the sample size and the growth rate of the sampled material.

In our study, we used two common circumpolar bivalves, the Greenland cockle (*S. groenlandicus*) and the hairy cockle (*C. ciliatum*), deployed on oceanographic moorings within two fjords, with different oceanographic conditions, situated in the Svalbard archipelago. The objectives of this study were to: 1) establish sub-annual shell growth models for subsequent element/Ca analyses and interpretations, 2) study the effects of temperature and food availability on sub-annual shell growth patterns, and 3) test the hypothesis that the trigger for the winter growth line is reduced food supply [15], using an oceanographic dataset with sub-annual resolution.

Materials and Methods

Bivalves, mooring sites and oceanographic instrumentation

Oceanographic moorings are maintained in Kongsfjorden (K, 78°57.4'N 11°49.6'E, depth 170 m) and Rijpfjorden (R, 80°18'N 22°20'E, depth 220 m), situated in Svalbard (Figure 1) [15, 49, 50].

Calcein-marked bivalve mollusks (*Serripes groenlandicus* and *Ciliatocardium ciliatum*) were placed in 7 mm plastic-mesh (Vexar L-32) baskets on each mooring in September 2009 and recovered one year later (Table 1). Originally, the bivalve mollusks were collected from Spitsbergenbanken in the Western Barents Sea (Figure 1) in August 2009 using a triangular dredge, after which they were held in flow-through seawater tanks for 4 weeks at the University Centre on Svalbard. Specimens were incubated in seawater with 125 mg L^{-1} of calcein dye for 24 h as described in Ambrose *et al.* [15] before deployment on the oceanographic moorings within both fjords (Table 1).

Kongsfjorden is located on the west coast of Spitsbergen and is influenced by the West Spitsbergen Current, which brings relatively warm Atlantic water into the fjord (Figure 1) [51]. The mooring site in Kongsfjorden is rarely covered by sea-ice. In contrast, Rijpfjorden is located on Nordaustlandet facing northward to the Arctic Ocean. It has an irregular sill and a broad, shallow shelf (depth 100–200 m) outside the fjord that extends approximately 100 km to the north before the shelf-break of the polar basin [52]. Consequently, Rijpfjorden is strongly influenced by cold Arctic currents and is seasonally ice covered [50,52]. The entire water column in Rijpfjorden has a temperature of -1.9 °C for 5-6 months each year during which the fjord is typically ice-covered [52]. Despite the shallow sill, the fjord is episodically affected by Atlantic water inflow events, leading to occasional rapid temperature and salinity fluctuations [53].

Temperature data loggers (HOBO TidbiT v2, accuracy $\pm$ 0.2 °C) mounted on the baskets containing bivalves recorded temperature every 10 to 40 min throughout the deployment period. Fluorometers (Seapoint Sensors, Inc.) and CTDs (37-SM MicroCAT, Sea-Bird Electronics) that were located adjacent to the baskets on the moorings (Table 1) measured fluorescence and conductivity (as a proxy for salinity) every second hour. The fluorometers were used with manufacturer's calibrations to provide estimates of seawater chlorophyll *a* concentration [54]. Since fouling or instrument drift may have affected the absolute voltage readings, a fluorescence index (FLI) was created by normalizing the voltage acquired from the fluorometers to the highest voltage recorded over the deployment period [15]. Daily averages of temperature and salinity were calculated from the mooring instrument data and used further in predicting $\delta^{18}O$ values for bivalve mollusk shell aragonite and data analyses.

Bivalve shell $\delta^{18}O$ measurements using SIMS

Individuals with the most growth (1.7–4.0 mm in shell length) during the deployment period were selected for $\delta^{18}O$ analyses. Samples from the basket at 15 m depth within Kongsfjorden were not analyzed for $\delta^{18}O$ values due to the lack of salinity measurements adjacent to the basket (Table 1). Shell height of each bivalve was measured from the umbo to the ventral margin, along the maximum growth axis, immediately after recovery (Figure 2). Next, soft tissue was removed, and the shells were dried at room temperature. Shells were stored dry until being embedded in epoxy resin and sectioned along the maximum growth axis using a Buehler Isomet low-speed saw, as described by Ambrose *et al.* [15] (Figure 2). The sections were then polished with a gradually finer sequence of sandpapers and finished using canvas with 1.5 μm AlO_2 powder. In order to locate the calcein line marking the beginning of the field deployment, the polished shell sections were photographed using fluorescent imaging (460–500 nm) with a Nikon episcopic compound microscope equipped with a Ludl motorized stage. Afterwards, the polished shell

slabs were glued on petrographic slides using epoxy resin. The shells were cut and the resulting thick sections polished to a thickness of 2.0±0.1 mm. Growth increments during the mooring period were then cut and the pieces mounted on epoxy mounts with a diameter of 25 mm. The mounts were coated with ca. 30 nm of gold and analyzed for *in situ* δ^{18}O values using secondary ion mass spectrometer (SIMS). Approximately one SIMS analysis was completed per 100 μm of shell growth until the prominent winter growth band, after which samples were taken at higher spatial resolution until the calcein line indicating the beginning of the mooring deployment period (Figure 3).

 In situ oxygen-isotope ratio analyses were conducted using a CAMECA IMS 1280 large geometry SIMS at the NordSIM facility in Stockholm, Sweden. The analytical protocol closely followed the standard δ^{18}O measurement procedure described for zircon by Whitehouse and Nemchin [55], which is applicable with little modification to other O-bearing minerals. A critically focused Cs^+ primary beam with 20 keV impact energy and ca. 2 nA beam current was used to sputter the sample, with charge build-up mitigated by use of a normal-incidence, low-energy electron flooding gun. Each analysis consisted of an initial pre-sputter over a rastered 20 μm area to remove the gold coat and attain stable secondary ion emission. A 10 μm primary raster was retained for data acquisition in order to homogenize the primary beam profile on the sample; together with the intrinsic primary beam spot diameter, this approach resulted in average sample spot diameter of 20.2 ± 2.6 μm (SD, n = 450). Following centering of the secondary beam in the field aperture (field of view on the sample of 30 μm with 90x magnification transmission ion optics) the ^{16}O (c. 2x10^9 cps) and ^{18}O ion beams were mass filtered at a mass resolution of ca. 2500 (M/ΔM) and analyzed simultaneously by Faraday detectors with amplifiers housed in an evacuated, temperature stabilized chamber. The secondary magnetic field was locked at high stability using an NMR field sensor operating in regulation mode. All pre-sputter, beam centering, and data acquisition steps were automated in the run definition.

 Fully automated sequences consisted of 2–3 measurements of the reference carbonate, Brown Yule Marble calcite (BYM, kindly provided by J. Craven, University of Edinburgh, from an original donation by B. Gilletti, Brown University) separating 5–7 measurements of the shell material. The regularly interspersed BYM measurements enabled correction of measured isotope ratios for any drift during the run sequence. Three separate bulk analyses of the BYM calcite yielded an average δ^{18}O$_{VPDB}$ of -6.55 ± 0.13 ‰ (SD, J. Craven personal communication), in good agreement with other reported values for the same material (e.g. Clemens *et al.* [56] who report -6.56 ± 0.06 ‰) and this value was used for calculation of instrumental mass fractionation (IMF) and normalization of shell δ^{18}O$_{VPDB}$ values. The average repeatability (internal precision) of 679 analyses was 0.11 ‰ (SE on 12 4-second cycles; range from 0.05 to 0.31 ‰), while the average reproducibility (external precision) of 229 drift-corrected BYM analyses from four sessions was 0.14 ‰ (SD, range from 0.12 to 0.17 ‰). The uncertainty on each reported δ^{18}O value results from propagation of the repeatability with the reproducibility for the specific analytical session. SIMS data is available as supplementary information (Data S2). All δ^{18}O values in this study are given relative to VPDB unless specified otherwise.

Predicted bivalve shell aragonite δ^{18}O values

Predicted δ^{18}O values in biogenic aragonite were calculated from known seawater temperature and salinity records based on a modified version of the equation formed by Grossman and Ku [31]. The equation was corrected for the Vienna normalized scale by subtracting 0.27 [57–59] from the original equation:

$$T = 20.60 - 4.34[\delta^{18}O_{aragonite} - (\delta^{18}O_{water} - 0.27)] \tag{1}$$

where T is temperature in °C and δ^{18}O values for aragonite and seawater expressed relative to Vienna Pee Dee Belemnite (VPDB) and Vienna Standard Mean Ocean Water (VSMOW), respectively. Rearranging this equation and simplifying the constants allows prediction of the δ^{18}O values in bivalve mollusk shell aragonite according to:

$$\delta^{18}O_{aragonite\ VPDB}(‰) \approx -0.23\ T(°C) + \delta^{18}O_{water\ VSMOW}(‰) + 4.48 \tag{2}$$

Temperature measurements were acquired from the temperature loggers deployed in each basket within each fjord. Predicted δ^{18}O values for seawater were calculated using daily salinity measurements from the mooring CTDs (Table 1), and the salinity–$\delta^{18}O_w$ mixing-line equation for Kongsfjorden from MacLachlan *et al.* [30]:

$$\delta^{18}O_{water\ VSMOW}(‰) = 0.43\ Salinity - 14.68 \tag{3}$$

Prediction intervals (95% level) for predicted bivalve shell δ^{18}O values were calculated using average propagated external and internal error for each basket as standard deviation and an assumption of normal distribution. Uncertainties in δ^{18}O equations [30, 31] were not considered and the actual prediction intervals could be wider.

Measurement of SIMS sample spot distances along bivalve shell sections

The measurement technique developed for this study estimates the location of SIMS δ^{18}O sample spots relative to the historical location of the shell margin along an axis approximately perpendicular to the direction of growth (called measurement axis; Figure 3). In principle, the locations where growth lines reached the shell surface were first projected to the measurement axis (L_1 and L_2; Figure 4). Next, centroids of each sample spot were related to the closest growth lines on both sides of the sample spot by a distance ratio d_1/d_2 (Figure 4). This distance ratio was then scaled to the projected points (L_1 and L_2) along the measurement axis, such that the relative distance to the adjacent growth lines remained the same ($d_1/d_2 = d_{L_1}/d_{L_2}$). Finally, positions of the scaled sample spots along the measurement axis were measured from the point where the shell margin was projected to the measurement axis (Figure 3). The procedure was repeated for the closest points to L_1 and L_2 along the perimeter of a sample spot to estimate the extent to which a sample was averaged [48, 60].

Growth lines were first identified from high resolution photographs of polished thick sections before SIMS and LA-ICP-MS sampling and compared to high resolution photographs of the sections after sampling. Identified growth lines and sample spots were then marked using ImageJ [61] and imported to R [62] using RImageJROI package [63]. The spatstat package [64]

240 was used to calculate the distances as described above. The resulting R functions were compiled
241 to the sclero package [65] and the work-flow is described in detail in the associated tutorial [66].
242 The distances given by the sclero package were afterwards inverted to correspond to the direction
243 of growth (Figure 3). Hence, the distances included in the figures are given along the measurement
244 axis, starting from the calcein line.

Alignment of predicted and measured intra-shell δ^{18}O profiles

246 Sub-annual growth patterns for *S. groenlandicus* and *C. ciliatum* were determined by aligning
247 the SIMS-measured δ^{18}O values with predicted δ^{18}O values using dynamic time warping (DTW).
248 The DTW method consists of algorithms that align and compare temporal sequences, which
249 might vary in time or speed (i.e. along the x-axis) [67–70]. Dynamic time warping was run
250 using the dtw package [69] for R. In DTW, the alignment of reference (predicted bivalve shell
251 δ^{18}O values in this study) and query (SIMS-measured δ^{18}O profiles) indexes are constrained by
252 algorithms called "step pattern" [69, 71]. The chosen step pattern (*symmetric2*) allowed flexible
253 alignment of a query index along the reference index. A detailed description of DTW alignment
254 procedure used in this study is presented in Text S1.

255 In brief, SIMS-measured δ^{18}O values were first standardized to the maximum and minimum
256 value of a predicted δ^{18}O profile due to the offset between SIMS-measured and predicted δ^{18}O
257 values (possible reasons for the offset are discussed later). Such standardization required two
258 assumptions: 1) maximum and minimum δ^{18}O value over the predicted δ^{18}O profile (mooring
259 deployment period) was sampled along each shell, and 2) SIMS-measured δ^{18}O values along each
260 shell section were consistently related to predicted δ^{18}O values within some random error (signal
261 noise). Oxygen-isotope values predicted for the first and last day of mooring deployment were
262 added as standardized δ^{18}O values for the initial calcein mark (d = 0 μm) and the shell margin
263 in the measured profile, respectively. Next, measured δ^{18}O profiles were linearly interpolated
264 such that the length a query index matched with that of the reference index, which consisted of
265 daily predictions of δ^{18}O in shell aragonite. Finally, the uncertainty of aligned query index values
266 was estimated by random sampling of distances within the minimum and maximum extent of
267 each SIMS sample spot (Figure 4). The resulting permutation allowed estimation of uncertainty
268 introduced by several possible DTW alignments in resulting growth models: the procedure not
269 only changed the distance of each measured value, but could also change the order, if maximum
270 and minimum limits of adjacent samples overlapped. The permutation was repeated 500 times
271 to estimate the maximum and minimum extent of each SIMS sample spot over time and to
272 calculate 95% quantiles for growth models.

273 Predicted δ^{18}O values for 26 m depth within Rijpfjorden decreased sharply during the ice-
274 formation, increased again a week later only to decrease to the levels lasting until mid-July
275 (Figure 5). This δ^{18}O fluctuation interfered with δ^{18}O profile alignment resulting to inadequate
276 DTW alignments. It is likely that this fluctuation was not representatively sampled in analyzed
277 shells, as the fluctuation took place during the winter with assumed slow shell growth (likely
278 over couple of μm [15]). Consequently, this fluctuation was removed from the reference index
279 used for DTW by linearly interpolating daily values using a δ^{18}O value before (2009-12-23) and
280 after (2010-02-07) the fluctuation. The fit of the SIMS-measured δ^{18}O values with predicted
281 δ^{18}O values after DTW alignment was quantified using linear regressions (Predicted δ^{18}O $\sim$

282 Measured δ^{18}O). Additionally, the range of days for which each measured δ^{18}O value was aligned
283 during 500 permutations (referred to as "accuracy") was used to illustrate the uncertainty in the
284 resulting DTW alignments.

Relationships between shell growth rate and mooring recordings

286 Weekly growth rates for each bivalve shell were calculated from the sub-annual growth models
287 using the DTW aligned centroid values. Two individuals (J and K) showed anomalously low δ^{18}O
288 values towards the ventral margin leading to implausible growth models; these two specimens were
289 removed from further growth rate analyses. The effects of seawater temperature, fluorescence
290 index and salinity values (fixed effects) to shell growth rate (response variable) were assessed
291 using linear mixed effects regression models (LMM). Relationships between shell growth rate and
292 the fixed effects was logarithmic, and consequently shell growth rate was logarithm transformed
293 prior analyses. Individual bivalve shells (termed "Samples" in consequent tables) and weeks from
294 deployment were used as crossed random effects assuming a random intercept and a constant
295 slope in LMMs [72]. Marginal coefficient of variation (R_m^2; [73]) was used to examine the variance
296 explained by each response variable separately (Model 1; see Text S2). The significance and
297 relative effects of each fixed effect on the growth rate were calculated using standardized values
298 of temperature, fluorescence index and salinity (each variable was centered to their means and
299 scaled to their standard deviations). The significance of these model parameters was estimated
300 using Satterthwaite approximation for denominator degrees of freedom [74] (Model 2; see Text
301 S2). Linear mixed models were calculated using the lme4 [75] and lmerTest packages [76], and
302 R_m^2 values using the MuMIn package [77]. All statistics were run using R statistical programming
303 environment [62].

Results

Seawater mooring data

306 Seawater temperature in Kongsfjorden ranged between –1.8 and 5.1 °C, with highest temperatures
307 at the beginning (September to December 2009) and the end (mid-July to September 2010) of the
308 mooring deployment period (Figure 5A). Kongsfjorden experienced three Atlantic water inflow
309 events during October 2009 and January and March 2010 (Figure 5A), as indicated by abrupt
310 increases in seawater temperature and salinity (Figure 5B). Except for these events, salinity
311 was relatively stable throughout the deployment period, ranging between 33.3 and 35.0. The
312 mooring site in Kongsfjorden was not ice-covered during the deployment period. Rijpfjorden
313 experienced seawater temperatures between –1.9 and 4.8 °C, and the fjord was ice-covered from
314 mid-February until mid-July (inferred from mooring ADCP data as described in Wallace et
315 al. [50], and confirmed from ice charts [78]). Seawater temperatures were similar at both measured
316 depths within Rijpfjorden until late August, when the surface layer cooled by approximately
317 3 °C relative to the deeper (25 m) layer. Rijpfjorden experienced melt-water induced salinity
318 fluctuations ranging between 30.5 and 33.5 from September 2009 until November and again from
319 July to September 2010 (Figure 5B).

320   Predicted δ^{18}O in bivalve shell aragonite varied between 2.9 and 4.9 ‰ in Kongsfjorden,

between 2.1 and 5.1 ‰ at 10 m depth in Rijpfjorden, and between 3.1 and 5.0 ‰ at 26 m depth in Rijpfjorden (Figure 5C). The δ^{18}O profiles gradually increased from September 2009 until mid-April 2010 in Kongsfjorden, and until July 2010 in Rijpfjorden. After the maximum values were attained, predicted δ^{18}O values started to gradually decline in Kongsfjorden, whereas Rijpfjorden showed a more dramatic drop: predicted δ^{18}O values decreased from maximum values to minimum values within two months (Figure 5C). Prediction intervals (95% level) for predicted δ^{18}O values were $\pm$ 0.40 ‰ in Kongsfjorden, 0.35 ‰ for the 15 m basket in Rijpfjorden, and 0.41 ‰ for the 25 m basket in Rijpfjorden. These values indicate likely non-detectable δ^{18}O differences for SIMS-measured values in Kongsfjorden from mid-January until May and for Rijpfjorden from December until mid-June. The fluorescence index was close to zero prior to a dramatic increase during the spring to early summer (Figure 5D); the first fluorescence peak occurred earlier in Kongsfjorden (April) than in Rijpfjorden (mid-June).

SIMS-measured shell δ^{18}O profiles and alignment

SIMS-measured bivalve shell δ^{18}O values exhibited an increase from the calcein mark until or right after the winter growth band, after which δ^{18}O values decreased gradually until the margin (Figure 6). This decrease was of higher magnitude in Rijpfjorden than in Kongsfjorden. Maximum δ^{18}O values among shell sections within a basket were relatively consistent, the maximum difference of 1.14 ‰ between sample A and C from Kongsfjorden (Table 2). In contrast, minimum values varied more: two *C. ciliatum* shells (J and K; Table 2) from the 25 m basket in Rijpfjorden had an anomalously low minimum δ^{18}O values (down to -8.7 ‰) towards the shell margin.

Trends in the SIMS-measured shell δ^{18}O profiles matched with the changes in the predicted δ^{18}O values, assuming relatively slow growth until the winter growth band and faster growth during the time of decrease in SIMS-measured δ^{18}O values (Figures 7 and 8). The dynamic time warping (DTW) procedure provided significant regressions (p < 0.001) between predicted δ^{18}O values for shell aragonite and the centroids of SIMS-measured δ^{18}O values, with coefficients of determination (R^2) ranging from 0.53 to 0.99 (Table 2). SIMS-measured δ^{18}O values were on average 5.45 $\pm$ 0.22 (SE, n = 12) ‰ lower than the predicted δ^{18}O values (Table 2). The average accuracy of aligned SIMS spots varied between 4 and 35 days among samples (Table 2).

Sub-annual bivalve shell growth models

Shell growth models resulting from DTW alignment exhibited two growth seasons during the mooring deployment: autumn (September to November–December) and summer (May–July to September; Figure 9). Two shells from Kongsfjorden [a *C. ciliatum* (C) and a *S. groenlandicus* (B)] grew considerably during the autumn growth season (43 and 52 % of their total annual growth increments), whereas the other shells grew the most during July–August, irrespective of fjord or species (Figures 9 and 10). There were no apparent differences in modeled growth patterns between species (Figure 9). Estimation of the timing of the start and end of the prominent winter growth band was associated with a high uncertainty for both fjords due to slow shell growth rate and resulting low number of SIMS δ^{18}O sample spots taken adjacent to the winter growth bands (Figure 6). Relatively constant predicted δ^{18}O values between February

and mid-June in Rijpfjorden further increased the uncertainty in assigning dates to the start and end of the winter growth band (Figure 5). Nevertheless, the growth models indicated that winter growth bands could have ended approximately simultaneously with the onset of summer growth in both fjords (Figure 9). Samples J and K (*C. ciliatum* from the basket at 25 m depth within Rijpfjorden) with anomalously low measured $\delta^{18}O$ values have different growth models than other samples from Rijpfjorden, with most of their estimated shell growth occurring in the middle of the winter (Figures 8 and 9).

Shell growth rate was more seasonal in Rijpfjorden, with higher growth rates during July–August (up to 1141 μm w^{-1}), than in Kongsfjorden where the growth season lasted longer than in Rijpfjorden (7 months, Figure 10). Weekly averaged temperature provided significant regressions with logarithm of weekly shell growth marginal R^2 ranging from 0.30 to 0.40 among baskets (Table 3). By comparison, weekly averages of the fluorescence index demonstrated significant relationships with logarithm of shell growth rate only in Kongsfjorden marginal R^2 being 0.11. Salinity did not demonstrate significant relationships with shell growth rate. The relative effect estimates demonstrated that the effect of temperature on logarithm of growth rate was twice the magnitude compared to the effect of fluorescence (Table 3).

Discussion

The dynamic time warping (DTW) alignment of SIMS-measured $\delta^{18}O$ values to predicted $\delta^{18}O$ values lead to adequate sub-annual growth models in 9 of 11 studied shells (Figure 7, Table 2). These growth models suggested that shell growth occurs between May and December within Kongsfjorden and between mid-June and November in Rijpfjorden (Figure 9). Furthermore, the winter growth band most likely marked the slow growth periods in both fjords (Figure 9). The results further indicated that food availability sets the temporal limits for growth season, whereas temperature partly controls shell growth rate when a food source is sufficient (Figure 10, Table 3). Consequently, our results confirm the hypothesis by Ambrose *et al.* [15] that the winter growth lines can be used as proxies of the time period when a food supply is not sufficient to sustain shell growth.

Sub-annual shell growth patterns

Alignment of measured $\delta^{18}O$ profiles with predicted $\delta^{18}O$ values suggested sub-annual growth patterns that are characterized by shell growth commencing during the phytoplankton bloom, highest shell growth rate one to two months after the peak of the phytoplankton bloom, and a growth cessation starting from November–December in both fjords and both bivalve species (Figures 9 and 10). Growth of both species commenced approximately six weeks earlier within the warmer and more Atlantic water influenced Kongsfjorden, compared to Rijpfjorden (Figure 10) which is typically dominated by Arctic water masses [51–53]. Most of the shell growth in Rijpfjorden specimens occurred over a short time period, from late June until mid-August, whereas the growth season within Kongsfjorden was longer, i.e. beginning in May and ending in November (Figure 10). Consequently, shell growth models indicated a shorter duration shell growth hiatus for Kongsfjorden ($\sim$5 months) compared to Rijpfjorden ($\sim$7–8 months). These shell growth patterns, modeled from measured versus predicted $\delta^{18}O$ profiles, are plausible. *S.*

groenlandicus and *C. ciliatum* are both filter-feeders and, because these bivalves were deployed on moorings in the water column, most of their diet likely consisted of phytoplankton and/or ice-algae. Primary production in the Arctic region is highly seasonal; very low or no food for filter-feeding bivalves is available during winter, before light-levels sufficient for photosynthesis return in the spring and lead to a phytoplankton or ice-algae bloom [53, 79]. Timing of the phytoplankton bloom at high latitudes is regulated by the angle of the Sun at a given latitude, by water-mass stratification, and by the occurrence of sea-ice, which can delay the bloom by several months [80]. The fluorescence index in our study can be used as a proxy for the timing and relative intensity of phytoplankton bloom events within the two fjords that were investigated [15, 81].

Since Kongsfjorden was ice-free during the deployment period, the timing of its phytoplankton bloom was relatively predictable, beginning in April, reaching its maximum in early May, and turning to post-bloom by June, as indicated by mooring fluorescence readings at 36 m depth (Figure 10). Such bloom dynamics correspond to what is known for Kongsfjorden from previous studies [79, 82, 83]. Our reconstruction of shell growth starting a month after the return of a food source is reasonable considering that somatic growth and replenishment of energy reserves is likely to precede shell growth [84, 85]. Growth models for shells deployed within Kongsfjorden show a slower growth during June, compared to earlier in the season (Figure 10). Although this could be explained by an imprecision in the DTW alignment, maturation of gonads could also have affected the shell growth rate: *S. groenlandicus* specimens deployed in Kongsfjorden were 31 mm and 39 mm in shell length during deployment and therefore likely sexually mature [86]. The timing of spawning in *S. groenlandicus* on Svalbard is not well documented, but specimens collected in May and held in aquaria at 2 °C spontaneously spawned in mid-June (Vihtakari, personal observation). The timing within laboratory aquaria matches with the time of slower shell growth observed in this field study. The *C. ciliatum* specimen from Kongsfjorden was likely not sexually mature (shell height only 21 mm) and differed from *S. groenlandicus* specimens in its shell growth pattern, with most shell growth taking place during the autumn (Figure 9). This interpretation of a large proportion of annual shell growth during autumn in Kongsfjorden is interesting (Figure 10). Even though our fluorescence data indicated a low abundance of chlorophyll *a* and thus photosynthesizing algae during the autumn (Figure 5D), the water column was likely to contain degrading phytoplankton and heterotrophic plankton that could have functioned as a food source for the bivalves [82, 87]. Bivalve shell growth during October to November has previously been reported for *Chlamys islandica* from South-East Greenland [88] and for *Arctica islandica* from the North Sea [14].

Rijpfjorden was ice covered until mid-July and consequently the timing of the phytoplankton bloom there was more difficult to establish than in Kongsfjorden. Seawater temperature records indicated sea-ice melt beginning in mid-June, coinciding with a peak in fluorescence index (Figure 5A and D). It is possible that this first peak in fluorescence was caused by ice-algae released to the water column due to sea ice melt. Alternatively, the phytoplankton bloom could have taken place during the ice melt in crevasses formed during the melting process [53]. Nevertheless, the fluorescence peak in mid-June clearly indicates a major food source for bivalves deployed on the Rijpfjorden mooring (Figure 5D). Shell growth in Rijpfjorden commenced almost simultaneously with this food occurrence, suggesting that the bivalves could have already replenished their energy reserves (Figure 10). Low fluorescence readings prior to June could indicate that some ice-algae was available within the water column, starting from April–May (Figure 5D), as also

reported by Leu *et al.* [53]. High fluorescence index values within Rijpfjorden from mid-August until the end of the bivalve deployment period (mid-September) are difficult to explain, but indicate a supply of an algal food source throughout the summer period. Highest shell growth rates during late-July for both baskets in Rijpfjorden are likely over-estimates due to poor fitting of measured $\delta^{18}O$ values in the DTW alignments and therefore the low shell growth rates during August to September should be treated with caution. One *S. groenlandicus* specimen from the basket at 25 m depth within Rijpfjorden was likely mature (shell length 40 mm), whereas other specimens were not. Nevertheless, the sub-annual growth pattern did not remarkably differ from the other specimens from the same basket (solid line with the highest growth rate in October in Figure 9C).

Two samples from Rijpfjorden had anomalously low $\delta^{18}O$ values towards the ventral margin. The growth models for these two shells indicated 42 to 50 % of the total annual shell growth occured during the period between November and February, which is an unlikely scenario given the likely absence of food source. Even though we are unable to specify the definitive reasons for these low *in situ* SIMS-measured $\delta^{18}O$ values based on our dataset, growth models for these two shells are unrealistic and the samples thus have been excluded from further shell growth rate analyses (Figure 10, Table 3).

Effects of temperature and food availability on sub-annual shell growth rates

The overall weekly shell growth rates demonstrated significant relationships with measured weekly seawater temperature for all baskets with overall marginal R^2 of 0.29 (Table 3). Annual standardized shell growth index (SGI) of *S. groenlandicus* and *C. ciliatum* has previously been used as an environmental proxy, which has been linked to various climatic oscillation indexes [20–24]. Many of these studies have raised a fundamental question, i.e. whether it is food availability or seawater temperature that is the driving factor of shell growth rate and thereby correlation with the climatic indexes. Our data indicate that seawater temperature is an important contributing factor to shell growth in Arctic bivalves by controlling the metabolic rate of ectotherms, whereas food availability sets the limits for growth season, but does not necessarily correlate well with growth rate (Figure 10). Therefore, both food availability and seawater temperature are important factors regulating shell growth of Arctic bivalve mollusks, but if a food source is sufficient then, shell growth is likely to reflect variations in seawater temperature. Consequently, SGI is likely influenced by both, temperature and food availability, but also other factors that were not identified in this study.

Despite their uncertainties, our shell growth models indicate that the prominent winter growth bands were likely formed simultaneously with the shell growth cessation lasting from December until May within Kongsfjorden and from November until mid-June within Rijpfjorden (Figure 9). Food availability was the likely determinant controlling when shell growth commenced in the spring, as well as the slowing of shell growth during the autumn (Figure 10), and therefore our data support the hypothesis by Ambrose *et al.* [15] that winter growth bands can be used as a proxy of the timing of food abundance in *S. groenlandicus* and *C. ciliatum* grown on moorings in Svalbard. However, this finding does not necessarily apply directly to bivalve molluscs sampled from their natural habitats, since wave action and storms might resuspend sediments with potential food particles during winter and therefore provide a food source that can support shell

487 growth.

The offset between SIMS-measured $\delta^{18}O$ and predicted $\delta^{18}O$ values

489 Measured $\delta^{18}O$ values in bivalve shell aragonite were on average 5.5 ‰ lower compared to predicted
490 $\delta^{18}O$ values (Table 2), the latter derived by combining continuous seawater temperature and
491 salinity records with an established paleothermometry equation (Equation 2) [31, 59] and a
492 salinity–$\delta^{18}O$ relationship for Kongsfjorden (Equation 3) [30]. All paleothermometry equations
493 for biogenic carbonates have been generated using phosphoric acid digestion, which liberates
494 oxygen only from carbonate phases [31, 36, 43, 44]. In contrast, secondary ion mass spectrometry
495 (SIMS) is a surface (*in situ*) technique that sputters oxygen ions from all phases contained within
496 a shell sample, and SIMS-determined $\delta^{18}O$ values are often lower compared to the true isotopic
497 abundances due to instrumental mass fractionation (IMF) [37, 40]. Because reliable aragonite
498 SIMS-standards were not available, a calcite standard (Brown Yule Marble) was used in this
499 study, even though the bivalve shells consisted of aragonite. Previous SIMS studies of oxygen
500 isotope ratios in carbonates using similar instrumentation and analytical protocols to those in
501 this study have yielded conflicting results regarding the relative instrumental mass fractionation
502 between calcite and aragonite. Rollion-Bard *et al.* [37] report an average $IMF_{arg} - IMF_{cal}$ of
503 -2.8 ‰, further noting that this differed from session to session (range: -2.0 to -4.2 ‰) as a
504 result of unspecified instrument conditions. In contrast, Gabitov [42] report $IMF_{arg} - IMF_{cal}$ of
505 0.8 and 2.1 ‰ from two different sessions. It cannot be discounted that the marked differences
506 in IMF might be attributed to undetected heterogeneity in the aragonite reference materials
507 used or a dependence on trace element geochemistry as noted by Allison *et al.* [41] who report a
508 range in IMF_{arg} (calibrated using calcite) from 0.2 to -2.8 ‰ that might be dependent on Sr/Ca
509 ratios. The range of reported $\delta^{18}O$ values for *S. groenlandicus* shells using the phosphoric acid
510 digestion technique further indicate that the lower than predicted $\delta^{18}O$ values measured in this
511 study were likely due to the *in situ* SIMS technique: Measured $\delta^{18}O$ values in this study ranged
512 from -8.68 to 0.82 ‰ (Table 2), whereas predicted $\delta^{18}O$ values varied between 2.1 and 5.1 ‰.
513 Khim [25] reported annual mean *S. groenlandicus* shell $\delta^{18}O$ values to range from 0.1 to 3.4 ‰,
514 whereas predicted $\delta^{18}O$ values within a year varied between 0.3 and 2.7 ‰. Further, Carroll *et*
515 *al.* [18] reported $\delta^{18}O$ values ranging from 0 to 4 ‰ in *S. groenlandicus* shell aragonite. It is
516 possible that also other factors than differences in IMF contributed to the offset. These could
517 include organic-hosted oxygen [38] and carbonate-hosted sulphate [39]. SIMS sampling of these
518 two phases would supply oxygen to the measured signals and resultant $\delta^{18}O$ values, whereas the
519 predicted $\delta^{18}O$ values are only for the carbonate oxygen within aragonite.
520   Conventional oxygen-isotope ratio analyses would have required > 10 μg of aragonite powder
521 [32, 89], which could not have been milled at the required sampling resolution due to the small
522 growth increments and thin shells (200–500 μm) of the Arctic bivalves investigated in this
523 study (Figure 2). The aim of the present paper is not to use intra-shell SIMS-derived $\delta^{18}O$
524 values as an absolute seawater temperature proxy, but instead to use the observed intra-shell
525 variations to estimate the sub-annual shell growth patterns. Therefore, these causes of inaccuracy
526 when calibrating aragonite to calcite are not critical to our overall conclusions but, nonetheless,
527 highlight some of the pitfalls of the *in situ* methodology that remain to be properly resolved
528 by the SIMS analytical community. Oxygen-isotope ratio analysis of biogenic carbonates is a

standard method to reconstruct relationships between temperature and isotopic composition of seawater in paleoceanography [29, 31], and it has successfully been used for a wide range of bivalves [32, 47, 90] including *S. groenlandicus* [18, 25]. Therefore, shells from the same basket should in principle have similar δ^{18}O values at a given time during the mooring deployment.

Despite the limitations of the *in situ* SIMS measurements used in this study, the similarities in intra-shell δ^{18}O patterns (Figures 6) shell δ^{18}O profiles were characterized by similarities with respect to patterns adjacent to the winter growth band and margin (Figures 6 and 8). The resulting feasible sub-annual shell growth models (Figure 9), allow us to confidently assume that possible oxygen that was not in paleothermometric equilibrium was randomly distributed along the studied shells. This assumption is further supported by us failing to detect any obvious deviations in measured δ^{18}O values in association with sub-annual growth lines (Figures 6 and 8), which were considerably darker in color, and therefore likely to have contained more organic matrix [91]. Consequently, the methodology used was adequate to estimate sub-annual shell growth patterns of *S. groenlandicus* and *C. ciliatum*.

Novel methodology

Matching SIMS-measured δ^{18}O values to values predicted for aragonite could have been done in many different ways due to the offset in the magnitude of measured and predicted δ^{18}O values (Table 2), low variability in predicted δ^{18}O values during winter (Figure 5C), and noise in the measured δ^{18}O signal (Figures 6 and 8). Predicted and measured δ^{18}O profiles are often aligned manually in similar studies [32, 92], but manual alignment of δ^{18}O values is rarely an objective or reproducible method. The dynamic time warping (DTW) method was chosen for alignment because of its reproducibility and objective alignment of δ^{18}O values among bivalve shells (see Text S1). This study introduces a new digital method to align sample spots along chronologically deposited materials [65, 66]. The method not only aligns sample spots in relation to growth lines, which can vary in angle, curvature and distance, but also helps to estimate the area covered by a sample spot (Figure 4). Dynamic time warping combined with permutations using the spatial range each SIMS sample covered along the measurement axis allowed an incorporation of time-averaging error to the growth model outcomes [47, 48]. SIMS δ^{18}O measurements were associated with a considerable signal noise component, which led to an imprecision in dynamic time warping (DTW) alignments (Figures 7 and 8) and the resulting shell growth models (Figure 9). Consequently, the DTW alignment method performed with a variable degree of success, depending on the variability of the measured δ^{18}O profile, but in general resulted to plausible sub-annual shell growth models. We believe that the combination of the two methods used in this study will be useful for a wider research community, especially for time-series records with considerable intra-annual variability, and that these methods can be developed further.

Conclusions

Information on the sub-annual timing of visible growth band deposition is especially valuable for palaeoclimate proxy studies, since these marks can be used as anchors to create chronologies, if their deposition is connected to processes that take place predictably from year to year. Our results demonstrate that the prominent winter growth band in *S. groenlandicus* and *C. ciliatum*

is likely deposited during the time of low food supply, and this information can be used further in proxy studies to constrain seasonal shell growth patterns. Our results also indicate that when food supply is sufficient, the shell growth rate of studied bivalves is likely to correlate with seawater temperature indicating that temperature is an important driver of Arctic bivalve mollusk shell growth. Dynamic time warping is a promising approach to better containing sub-seasonal and annual growth patterns in bivalves. Together with the sample spot alignment method developed for this study, DTW algorithms allowed an estimation of time-averaging error associated with geochemical sampling of bivalve shells. This study demonstrates a need for calibration of *in situ* SIMS $\delta^{18}O$ analyses in biomineral carbonates, such as aragonitic bivalve mollusk shells, including comparisons with the conventional phosphoric acid digestion and gas source isotope ratio mass spectrometry methods, the evaluation of the contribution of organic- and sulfate-hosted oxygen [38,39] to the SIMS $\delta^{18}O$ signals, and most importantly, addressing the potential inaccuracy in IMF of aragonite reference materials for SIMS.

Acknowledgments

References

1. Grebmeier JM (2012) Shifting patterns of life in the Pacific Arctic and sub-Arctic seas. Ann Rev Mar Sci 4: 63–78.

2. Wassmann P, Duarte CM, Agustí S, Sejr MK (2011) Footprints of climate change in the Arctic marine ecosystem. Glob Chang Biol 17: 1235–1249.

3. ACIA (2004) Impacts of a warming Arctic: Arctic Climate Impact Assessment. Cambridge, UK: Cambridge University Press, 146 pp.

4. AMAP (2012) Arctic climate issues 2011: Changes in Arctic snow, water, ice and permafrost. SWIPA 2011 Overview report. Technical report, Arctic Monitoring and Assessment Programme (AMAP), Oslo, Norway. URL http://www.amap.no/documents/doc/arctic-climate-issues-2011-changes-in-arctic-snow-water-ice-and-permafrost/129.

5. AMAP (2013) AMAP Assessment 2013: Arctic Ocean acidification. Technical report, Arctic Monitoring and Assessment Programme (AMAP), Oslo, Norway. URL http://eprints.uni-kiel.de/22736/.

6. Kirtman B, Power S, Adedoyin J, Boer G, Bojariu R, et al. (2013) Near-term climate change: Projections and predictability. In: Stocker T, Qin D, Plattner GK, Tignor M, Allen S, et al., editors, Climate Change 2013: The Physical Science Basis Contribution of Working Group I to the Fifth Assessment Report of the Intergovernmental Panel on Climate Change, Cambridge, UK and New York, NY, USA: Cambridge University Press, chapter 11. pp. 953–1028.

7. Henderson GM (2002) New oceanic proxies for paleoclimate. Earth Planet Sci Lett 203: 1–13.

8. Felis T, Pätzold J (2004) Climate reconstructions from annually banded corals. In: Shiyomi M, Kawahata H, Koizumi H, Tsuda A, Awaya Y, editors, Glob Environ Chang Ocean L, TERRAPUB. pp. 205–227. URL http://www.terrapub.co.jp/e-library/kawahata/pdf/205.pdf.

9. Jones PD, Mann ME (2004) Climate over past millennia. Rev Geophys 42: 1–42.

10. Wanamaker AD, Hetzinger S, Halfar J (2011) Reconstructing mid- to high-latitude marine climate and ocean variability using bivalves, coralline algae, and marine sediment cores from the Northern Hemisphere. Palaeogeogr Palaeoclimatol Palaeoecol 302: 1–9.

11. Masson-Delmotte V, Schulz M, Abe-Ouchi A, Beer J, Ganopolski A, et al. (2013) Information from paleoclimate archives. In: Stocker T, Qin D, Plattner GK, Tignor M, Allen S, et al., editors, Climate Change 2013: The Physical Science Basis Contribution of Working Group I to the Fifth Assessment Report of the Intergovernmental Panel on Climate Change, Cambridge, UK and New York, NY, USA: Cambridge University Press, chapter 5. pp. 383–464.

12. Proctor CJ, Baker A, Barnes WL, Gilmour MA (2000) A thousand year speleothem proxy record of North Atlantic climate from Scotland. Clim Dyn 16: 815–820.

13. Sejr MK, Jensen KT, Rysgaard S (2002) Annual growth bands in the bivalve *Hiatella arctica* validated by a mark-recapture study in NE Greenland. Polar Biol 25: 794–796.

14. Schöne BR, Houk SD, Castro ADF, Fiebig J, Oschmann W, et al. (2005) Daily growth rates in shells of *Arctica islandica*: Assessing sub-seasonal environmental controls on a long-lived bivalve mollusk. Palaios 20: 78–92.

15. Ambrose Jr WG, Renaud PE, Locke V WL, Cottier FR, Berge J, et al. (2012) Growth line deposition and variability in growth of two circumpolar bivalves (*Serripes groenlandicus*, and *Clinocardium ciliatum*). Polar Biol 35: 345–354.

16. Schöne BR (2008) The curse of physiology - challenges and opportunities in the interpretation of geochemical data from mollusk shells. Geo-Marine Lett 28: 269–285.

17. Khim BK, Krantz DE, Cooper LW, Grebmeier JM (2003) Seasonal discharge of estuarine freshwater to the western Chukchi Sea shelf identified in stable isotope profiles of mollusk shells. J Geophys Res 108: 1–10.

18. Carroll ML, Johnson BJ, Henkes GA, McMahon KW, Voronkov A, et al. (2009) Bivalves as indicators of environmental variation and potential anthropogenic impacts in the southern Barents Sea. Mar Pollut Bull 59: 193–206.

19. Henkes GA, Passey BH, Wanamaker AD, Grossman EL, Ambrose Jr WG, et al. (2013) Carbonate clumped isotope compositions of modern marine mollusk and brachiopod shells. Geochim Cosmochim Acta 106: 307–325.

20. Sejr MK, Blicher ME, Rysgaard S (2009) Sea ice cover affects inter-annual and geographic variation in growth of the Arctic cockle *Clinocardium ciliatum* (Bivalvia) in Greenland. Mar Ecol Ser 389: 149–158.

21. Ambrose Jr WG, Carroll ML, Greenacre MJ, Thorrold SR, McMahon KW (2006) Variation in *Serripes groenlandicus* (Bivalvia) growth in a Norwegian high-Arctic fjord: evidence for local- and large-scale climatic forcing. Glob Chang Biol 12: 1595–1607.

22. Carroll ML, Ambrose Jr WG, Levin BS, Ryan SK, Ratner AR, et al. (2011) Climatic regulation of *Clinocardium ciliatum* (Bivalvia) growth in the northwestern Barents Sea. Palaeogeogr Palaeoclimatol Palaeoecol 302: 10–20.

23. Carroll ML, Ambrose Jr WG, Levin BS, Locke V WL, Henkes GA, et al. (2011) Pan-Svalbard growth rate variability and environmental regulation in the Arctic bivalve *Serripes groenlandicus*. J Mar Syst 88: 239–251.

24. Carroll ML, Ambrose Jr WG, Locke V WL, Ryan SK, Johnson BJ, et al. (2014) Bivalve growth rate and isotopic variability across the Barents Sea Polar Front. J Mar Syst 130: 167–180.

25. Khim BK (2002) Stable isotope profiles of *Serripes groenlandicus* shells. I. Seasonal and interannual variations of Alaskan Coastal Water in the Bering and Chukchi Seas. Geosci J 6: 257–267.

26. Wanamaker AD, Butler PG, Scourse JD, Heinemeier J, Eiríksson J, et al. (2012) Surface changes in the North Atlantic meridional overturning circulation during the last millennium. Nat Commun 3: 1–7.

27. Urey HC (1947) The thermodynamic properties of isotopic substances. J Chem Soc : 562–581.

28. Urey HC, Lowenstam HA, Epstein S, McKinney CR (1951) Measurement of paleotemperatures and temperatures of the Upper Cretaceous of England, Denmark, and the Southeastern United States. Geol Soc Am Bull 62: 399.

29. Epstein S, Buchsbaum R, Lowenstam HA, Urey HC (1953) Revised carbonate-water isotopic temperature scale. Bull Geol Soc Am 64: 1315–1326.

30. MacLachlan SE, Cottier FR, Austin WEN, Howe JA (2007) The salinity: δ^{18}O water relationship in Kongsfjorden, western Spitsbergen. Polar Res 26: 160–167.

31. Grossman E, Ku T (1986) Oxygen and carbon isotope fractionation in biogenic aragonite: temperature effects. Chem Geol 59: 59–74.

32. Goodwin DH, Cohen AN, Roopnarine PD (2010) Forensics on the half shell: a sclerochronological investigation of a modern biological invasion in San Francisco Bay, United States. Palaios 25: 742–753.

33. Goodwin DH, Gillikin DP, Roopnarine PD (2013) Preliminary evaluation of potential stable isotope and trace element productivity proxies in the oyster *Crassostrea gigas*. Palaeogeogr Palaeoclimatol Palaeoecol 373: 88–97.

34. Goodwin DH, Flessa KW, Schöne BR, Dettman DL (2001) Cross-calibration of daily growth increments, stable isotope variation, and temperature in the Gulf of California bivalve mollusk *Chione cortezi*: Implications for paleoenvironmental analysis. Palaios 16: 387–398.

35. Foster LC, Allison N, Finch AA, Andersson C, Ninnemann US (2009) Controls on δ^{18}O and δ^{13}C profiles within the aragonite bivalve *Arctica islandica*. Holocene 19: 549–558.

36. Ball JD, Crowley SF, Steele DF (1996) Carbon and oxygen isotope ratio analysis of small carbonate samples by conventional phosphoric acid digestion: sample preparation and calibration. Rapid Commun Mass Spectrom 10: 987–995.

37. Rollion-Bard C, Mangin D, Champenois M (2007) Development and application of oxygen and carbon isotopic measurements of biogenic carbonates by ion microprobe. Geostand Geoanalytical Res 31: 39–50.

38. Shiao JC, Itoh S, Yurimoto H, Iizuka Y, Liao YC (2014) Oxygen isotopic distribution along the otolith growth axis by secondary ion mass spectrometry: Applications for studying ontogenetic change in the depth inhabited by deep-sea fishes. Deep Sea Res Part I Oceanogr Res Pap 84: 50–58.

39. Yoshimura T, Tamenori Y, Kawahata H, Suzuki A (2014) Fluctuations of sulfate, S-bearing amino acids and magnesium in a giant clam shell. Biogeosciences 11: 3881–3886.

40. Shimizu N (1982) Isotope fractionation in secondary ion mass spectrometry. J Appl Phys 53: 1303.

41. Allison N, Finch AA, EIMF (2010) The potential origins and palaeoenvironmental implications of high temporal resolution δ^{18}O heterogeneity in coral skeletons. Geochim Cosmochim Acta 74: 5537–5548.

42. Gabitov RI (2013) Growth-rate induced disequilibrium of oxygen isotopes in aragonite: An *in situ* study. Chem Geol 351: 268–275.

43. Swart PK, Burns SJ, Leder JJ (1991) Fractionation of the stable isotopes of oxygen and carbon in carbon dioxide during the reaction of calcite with phosphoric acid as a function of temperature and technique. Chem Geol 86: 89–96.

44. Wendeberg M, Richter JM, Rothe M, Brand WA (2011) δ^{18}O anchoring to VPDB: calcite digestion with ^{18}O-adjusted ortho-phosphoric acid. Rapid Commun Mass Spectrom 25: 851–60.

45. Gillikin DP, De Ridder F, Ulens H, Elskens M, Keppens E, et al. (2005) Assessing the reproducibility and reliability of estuarine bivalve shells (*Saxidomus giganteus*) for sea surface temperature reconstruction: Implications for paleoclimate studies. Palaeogeogr Palaeoclimatol Palaeoecol 228: 70–85.

46. Schöne BR, Zhang ZJ, Radermacher P, Thebault J, Jacob DE, et al. (2011) Sr/Ca and Mg/Ca ratios of ontogenetically old, long-lived bivalve shells (*Arctica islandica*) and their function as paleotemperature proxies. Palaeogeogr Palaeoclimatol Palaeoecol 302: 52–64.

47. Goodwin D, Flessa K, Tellezduarte M, Dettman D, Schöne BR, et al. (2004) Detecting time-averaging and spatial mixing using oxygen isotope variation: a case study. Palaeogeogr Palaeoclimatol Palaeoecol 205: 1–21.

48. Beelaerts V, Ridder F, Schmitz N, Bauwens M, Dehairs F, et al. (2008) On the elimination of bias averaging-errors in proxy records. Math Geosci 41: 129–144.

49. Howe JA, Harland R, Cottier FR, Brand T, Willis KJ, et al. (2010) Dinoflagellate cysts as proxies for palaeoceanographic conditions in Arctic fjords. Geol Soc Spec Publ 344: 61–74.

50. Wallace MI, Cottier FR, Berge J, Tarling GA, Griffiths C, et al. (2010) Comparison of zooplankton vertical migration in an ice-free and a seasonally ice-covered Arctic fjord: An insight into the influence of sea ice cover on zooplankton behavior. Limnol Oceanogr 55: 831–845.

51. Svendsen H, Beszczynska-Møller A, Hagen JO, Lefauconnier B, Tverberg V, et al. (2002) The physical environment of Kongsfjorden – Krossfjorden, an Arctic fjord system in Svalbard. Polar Res 21: 133–166.

52. Søreide JE, Leu E, Berge J, Graeve M, Falk-Petersen S (2010) Timing of blooms, algal food quality and *Calanus glacialis* reproduction and growth in a changing Arctic. Glob Chang Biol 16: 3154–3163.

53. Leu E, Søreide J, Hessen D, Falk-Petersen S, Berge J (2011) Consequences of changing sea-ice cover for primary and secondary producers in the European Arctic shelf seas: Timing, quantity, and quality. Prog Oceanogr 90: 18–32.

54. Smith RC, Baker KS, Dustan P (1981) Fluorometric techniques for the measurement of oceanic chlorophyll in the support of remote sensing. Technical report, Scripps Institution of Oceanography, San Diego, USA. URL `http://escholarship.org/uc/item/4k51f7p0`.

55. Whitehouse MJ, Nemchin AA (2009) High precision, high accuracy measurement of oxygen isotopes in a large lunar zircon by SIMS. Chem Geol 261: 32–42.

56. Clemens SC, Prell WL, Sun Y, Liu Z, Chen G (2008) Southern Hemisphere forcing of Pliocene $\delta^{18}O$ and the evolution of Indo-Asian monsoons. Paleoceanography 23: PA4210:1–15.

57. Gonfiantini R (1984) Advisory group meeting on stable isotope reference samples for geochemicaland hydrological investigations. Technical report, IAEA, Vienna, Austria.

58. Hut G (1987) Consultant's group meeting on stable isotope reference samples for geochemical and hydrological investigations. Technical report, IAEA, Vienna, Austria.

59. Coplen T (1988) Normalization of oxygen and hydrogen isotope data. Chem Geol 12: 293–297.

60. Goodwin DH, Schöne BR, Dettman DL (2003) Resolution and fidelity of oxygen isotopes as paleotemperature proxies in bivalve mollusk shells: Models and observations. Palaios 18: 110–125.

61. Schneider CA, Rasband WS, Eliceiri KW (2012) NIH Image to ImageJ: 25 years of image analysis. Nat Methods 9: 671–675.

62. R Core Team (2014). R: A language and environment for statistical computing. R Foundation for Statistical Computing, Vienna, Austria. URL `http://www.r-project.org`.

63. Sterratt DC, Vihtakari M (2014). RImageJROI: read ImageJ Region of Interest (ROI) files. R package varsion 0.1. URL `http://cran.r-project.org/package=RImageJROI`.

64. Baddeley A, Turner R (2005) Spatstat: an R package for analyzing spatial point patterns. J Stat Softw 12: 1–42.

65. Vihtakari M (2014). sclero: measure growth patterns and align sampling spots in photographs. R package version 0.1. URL `https://github.com/MikkoVihtakari/sclero`.

66. Vihtakari M (2014). An R package for sclero- and dentrochronologists: sclero tutorial. URL `https://github.com/MikkoVihtakari/sclero/vignettes`.

67. Sakoe H, Chiba S (1978) Dynamic programming algorithm optimization for spoken word recognition. IEEE Trans Acoust 26: 43–49.

68. Senin P (2008) Dynamic time warping algorithm review. Technical report, Information and Computer Science Department, University of Hawaii, Honolulu, USA.

69. Giorgino T (2009) Computing and visualizing dynamic time warping alignments in R : the dtw package. J Stat Softw 31: 1–24.

70. Hladil J, Vondra M, Cejchan P (2010) The dynamic time-warping approach to comparison of magnetic-susceptibility logs and application to Lower Devonian calciturbidites (Prague Synform, Bohemian Massif). Geol Belgica 13: 385–406.

71. Müller M (2007) Dynamic time warping. In: Information Retrieval for Music and Motion, Berlin / Heidelberg, Germany: Springer, chapter 4. pp. 69–84.

72. Baayen R, Davidson D, Bates D (2008) Mixed-effects modeling with crossed random effects for subjects and items. J Mem Lang 59: 390–412.

73. Johnson PC (2014) Extension of Nakagawa & Schielzeth's R^2_{GLMM} to random slopes models. Methods Ecol Evol 5: 944–946.

74. SAS Technical Report R-101 (1978) Tests of hypotheses in fixed-effects linear models. Technical report, SAS Institute Inc., Cary, NC, USA.

75. Bates D, Maechler M, Bolker B, Walker S (2014). lme4: Linear mixed-effects models using Eigen and S4. R package version 1.1-7. URL http://cran.r-project.org/package=lme4.

76. Kuznetsova A, Bruun Brockhoff P, Haubo Bojesen Christensen R (2014). lmerTest: Tests for random and fixed effects for linear mixed effect models (lmer objects of lme4 package). R package version 2.0-11. URL http://cran.r-project.org/package=lmerTest.

77. Barton K (2014). MuMIn: Multi-model inference. R package version 1.10.5. URL http://cran.r-project.org/package=MuMIn.

78. Norwegian Meteorological Institute (2014). Icechart archive. Polar View – European Arctic node. URL http://polarview.met.no.

79. Daase M, Falk-Petersen S, Varpe O, Darnis G, Søreide JE, et al. (2013) Timing of reproductive events in the marine copepod *Calanus glacialis*: a pan-Arctic perspective. Can J Fish Aquat Sci 70: 871–884.

80. Leu E, Mundy CJ, Assmy P, Gabrielsen TM, Gosselin M, et al. (2014) Arctic spring awakening steering principles behind the phenology of vernal ice algae blooms. Prog Oceanogr In press.

81. Falkowski P, Kiefer DA (1985) Chlorophyll *a* fluorescence in phytoplankton: relationship to photosynthesis and biomass. J Plankton Res 7: 715–731.

82. Rokkan Iversen K, Seuthe L (2010) Seasonal microbial processes in a high-latitude fjord (Kongsfjorden, Svalbard): I. Heterotrophic bacteria, picoplankton and nanoflagellates. Polar Biol 34: 731–749.

83. Hodal H, Falk-Petersen S, Hop H, Kristiansen S, Reigstad M (2011) Spring bloom dynamics in Kongsfjorden, Svalbard: nutrients, phytoplankton, protozoans and primary production. Polar Biol 35: 191–203.

84. Lewis D, Cerrato R (1997) Growth uncoupling and the relationship between shell growth and metabolism in the soft shell clam *Mya arenaria*. Mar Ecol Prog Ser 158: 177–189.

85. Sejr MK, Petersen JK, Jensen KT, Rysgaard S (2004) Effects of food concentration on clearance rate and energy budget of the Arctic bivalve *Hiatella arctica* (L) at subzero temperature. J Exp Mar Bio Ecol 311: 171–183.

86. Kilada RW, Roddick D, Mombourquette K (2007) Age determination, validation, growth and minimum size of sexual maturity of the Greenland smoothcockle (*Serripes groenlandicus*, Bruguiere, 1789) in Eastern Canada. J Shellfish Res 26: 443–450.

87. Hegseth EN (1997) Phytoplankton of the Barents Sea - the end of a growth season. Polar Biol 17: 235–241.

88. Blicher ME, Rysgaard S, Sejr MK (2010) Seasonal growth variation in *Chlamys islandica* (Bivalvia) from sub-Arctic Greenland is linked to food availability and temperature. Mar Ecol Ser 407: 71–86.

89. Wanamaker AD, Kreutz KJ, Schöne BR, Introne DS (2011) Gulf of Maine shells reveal changes in seawater temperature seasonality during the Medieval Climate Anomaly and the Little Ice Age. Palaeogeogr Palaeoclimatol Palaeoecol 302: 43–51.

90. Wanamaker AD, Kreutz KJ, Borns HW, Introne DS, Feindel S, et al. (2006) An aquaculture-based method for calibrated bivalve isotope paleothermometry. Geochemistry, Geophys Geosystems 7: Q09011:1–13.

91. Schöne BR, Zhang Z, Jacob D, Gillikin DP, Tutken T, et al. (2010) Effect of organic matrices on the determination of the trace element chemistry (Mg, Sr, Mg/Ca, Sr/Ca) of aragonitic bivalve shells (*Arctica islandica*) – Comparison of ICP-OES and LA-ICP-MS data. Geochem J 44: 23–37.

92. Cardoso JF, Santos S, Witte JI, Witbaard R, van der Veer HW, et al. (2013) Validation of the seasonality in growth lines in the shell of *Macoma balthica* using stable isotopes and trace elements. J Sea Res 82: 93–102.
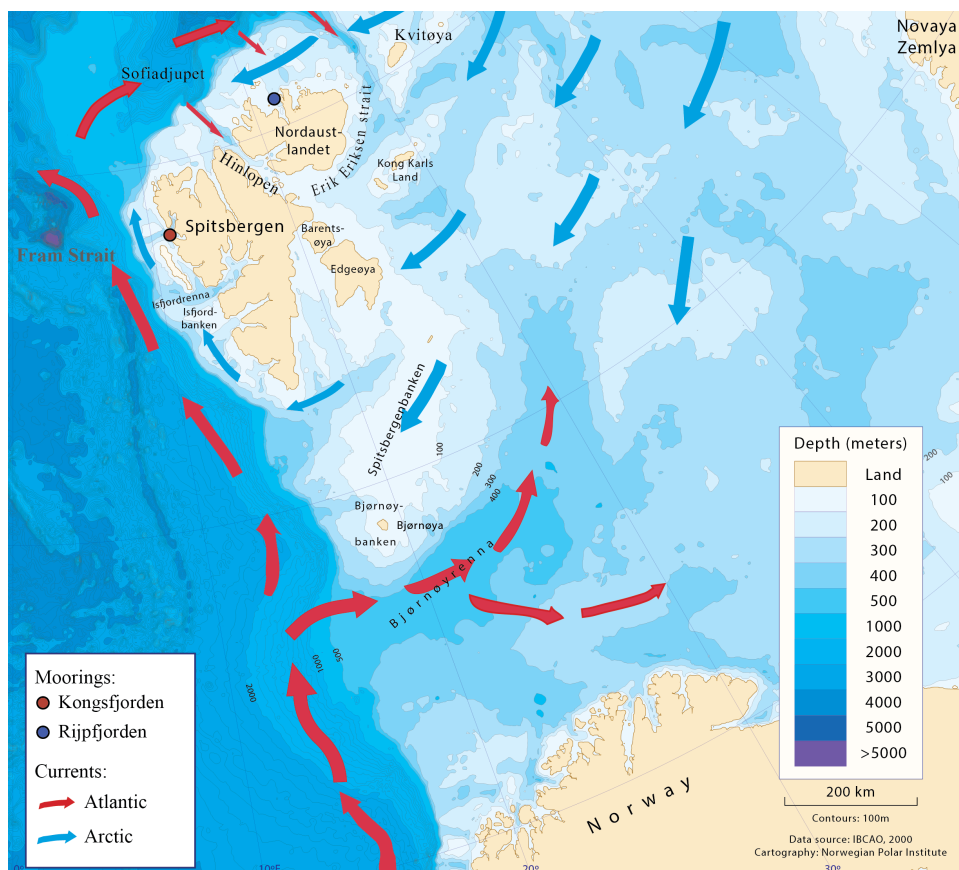
Figures

Figure 1. Map over Svalbard and Barents Sea. Bivalves were deployed on moorings in two fjords on Svalbard (marked with red and blue dot). Red arrows indicate Atlantic water brought by the West Spitsbergen current and blue arrows the cold currents dominated by Arctic water masses. Svalbard is located to the upper left. The map was made by Norwegian Polar Institute.
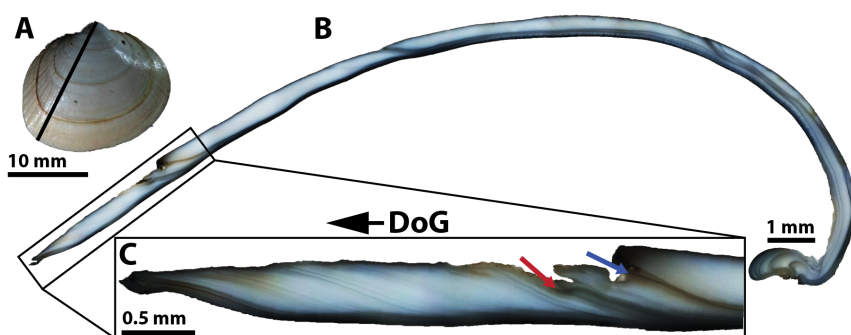
Figure 2. Schematics of growth line deposition in bivalves. A) *Serripes groenlandicus* shell with visible external growth lines. Black line demonstrates the maximum growth axis along which cross-sections were cut. **B)** Shell cross-section along the maximum growth axis showing annual growth lines starting from the inner edge and curving upwards towards the visible shell surface. **C)** Growth during the mooring deployment showing a disturbance growth line formed during deployment (blue arrow), a prominent opaque winter growth line (red arrow) and several weaker subannual growth lines. Growth lines are deposited in an angle to direction of growth (DoG). Each growth line marks an approximate historical location of the shell margin and can be traced along the shell section.
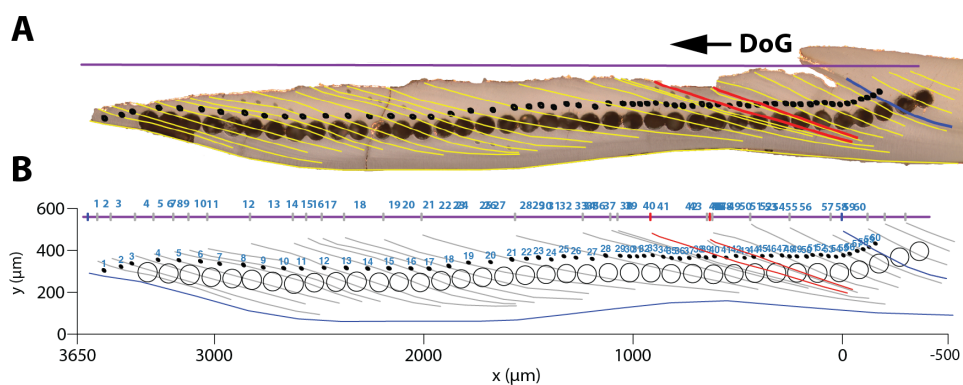
Figure 3. Example of SIMS sample spot alignment. A) Shell cross-section after SIMS (small black dots) sampling. Large holes are laser-ablation craters (unpublished data). Colored lines on the shell section indicate growth lines marked with ImageJ. The blue line represents the calcein mark, and red lines the beginning and the end of the winter growth band. Yellow lines are sub-annual growth lines used to align sample spots. Purple horizontal line represents the measurement axis along which sample spots were aligned. DoG = direction of growth. **B)** Resulting digital representation of the shell section. Black dots indicate the SIMS samples and blue numbers the sample number. Sample spots are aligned along the measurement axis (purple line) relative to growth lines as explained in Figure 4. Open large circles indicate the laser-ablation craters. Scales are similar for both sub-figures and axes scales in B indicate distance in μm. X-axis scale is converted and begins from the deployment (= calcein mark; blue line). Sample spot sizes are presented in actual size in B. SIMS spots are larger than in reality in A to make them visible.
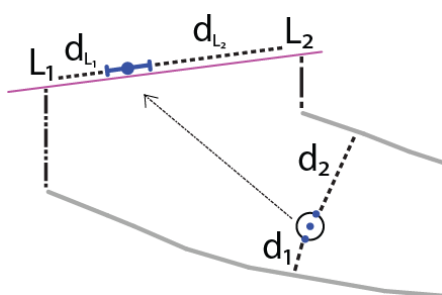
Figure 4. Alignment of SIMS sample spots along the measurement axis. Grey lines represent marked growth lines and open circle a sample spot. Centroid of the sample spot and the closest points to the growth lines along the perimeter (blue dots) were aligned such that $d_1/d_2 = d_{L_1}/d_{L_2}$ resulting to a segment along the measurement axis (blue dot with error bars). The dot represents the estimated location of the centroid and error bars the extent over which the SIMS sample was averaged.
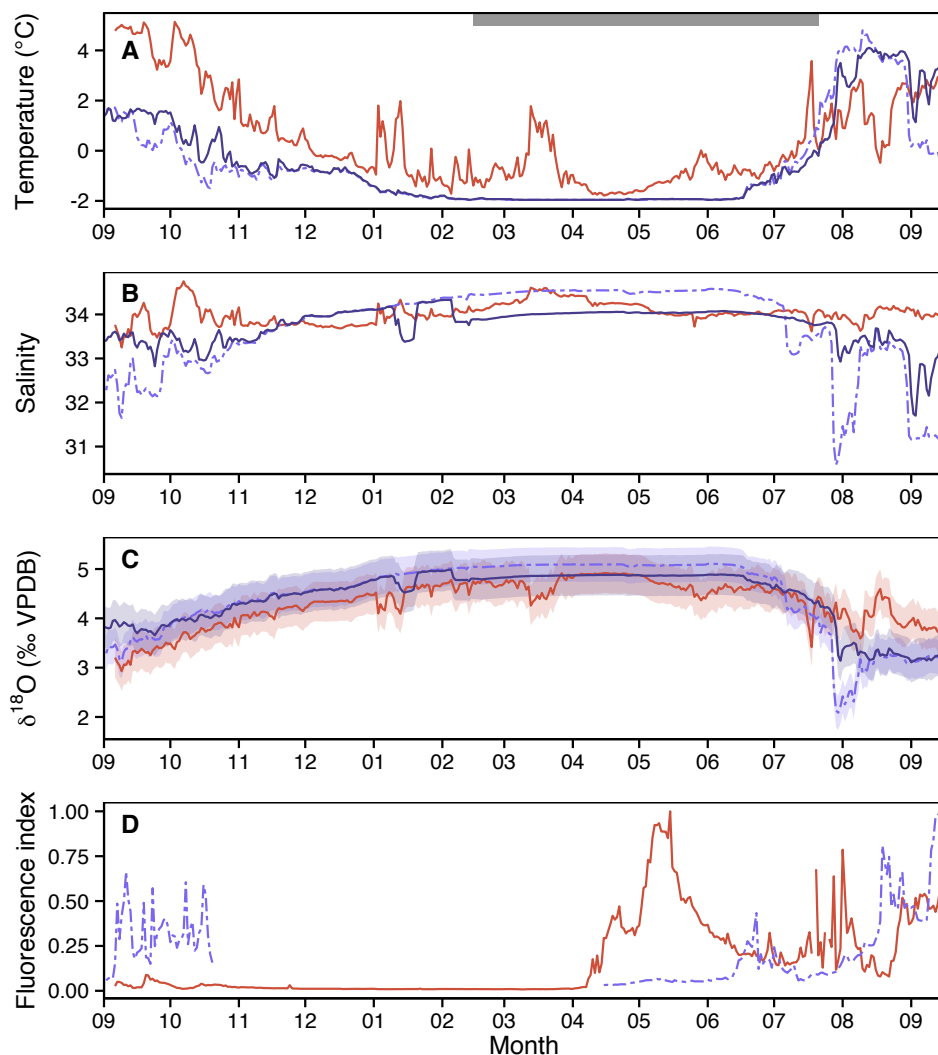
Figure 5. Seawater mooring data and predicted δ^{18}O values. A) Seawater temperature, **B)** salinity, **C)** predicted δ^{18}O, and **D)** fluorescence index over the deployment period as measured by mooring instruments. Red solid line indicates Kongsfjorden 36 m depth, dark blue solid line Rijpfjorden 26 m depth and light blue dashed line Rijpfjorden 10 m depth. Shading for δ^{18}O values illustrates 95 % prediction intervals for observed δ^{18}O values assuming a normal distribution and using propagated external and internal errors of SIMS samples averaged over each basket. The gray bar indicates the time of sea-ice cover in Rijpfjorden.
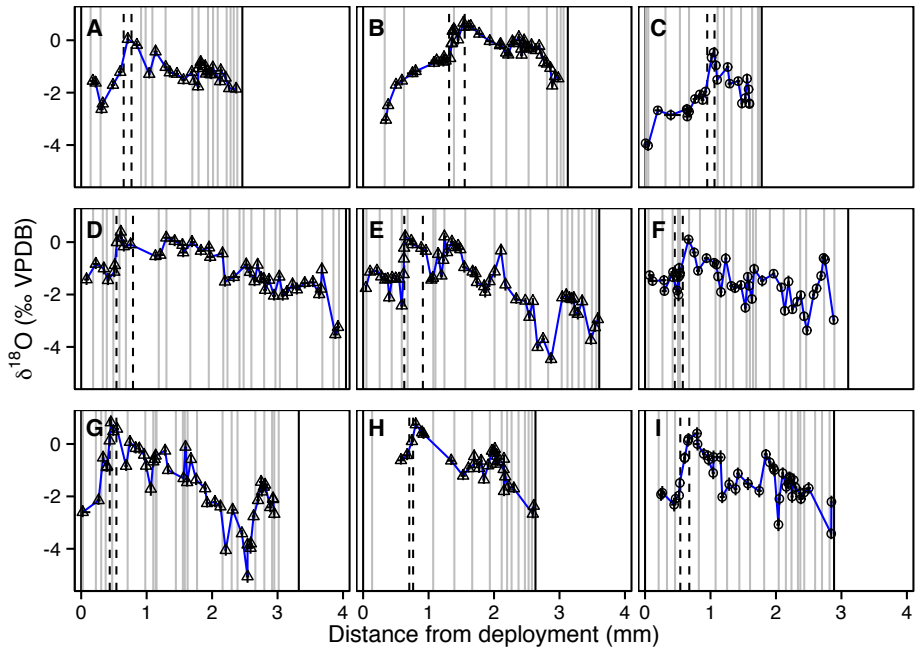
Figure 6. Measured δ^{18}O values scaled along the measurement axis. (**A-C**): The basket at 25 m depth in Kongsfjorden. (**D-F**): the basket at 15 m depth in Rijpfjorden. (**G-I**) The basket at 25 m depth in Rijpfjorden. Specimens C, F, and I are *C. ciliatum*, and the rest are *S. groenlandicus*. Vertical error bars indicate 2 standard deviations of the propagated internal and external instrument precision for SIMS δ^{18}O measurements. Horizontal error bars represent the estimated width of a sample spot along the measurement axis. First black vertical line from the left illustrates the calcein mark (=deployment in September 2009) and the second the shell margin (=recovery in September 2010). Dashed black vertical lines represent the beginning and the end of the prominent winter growth band. Grey vertical lines illustrate visible growth lines used in sample spot alignment (see Figure 3). Blue line represents interpolation trajectory that was used to align measured δ^{18}O values with predicted δ^{18}O values (see Text S1).
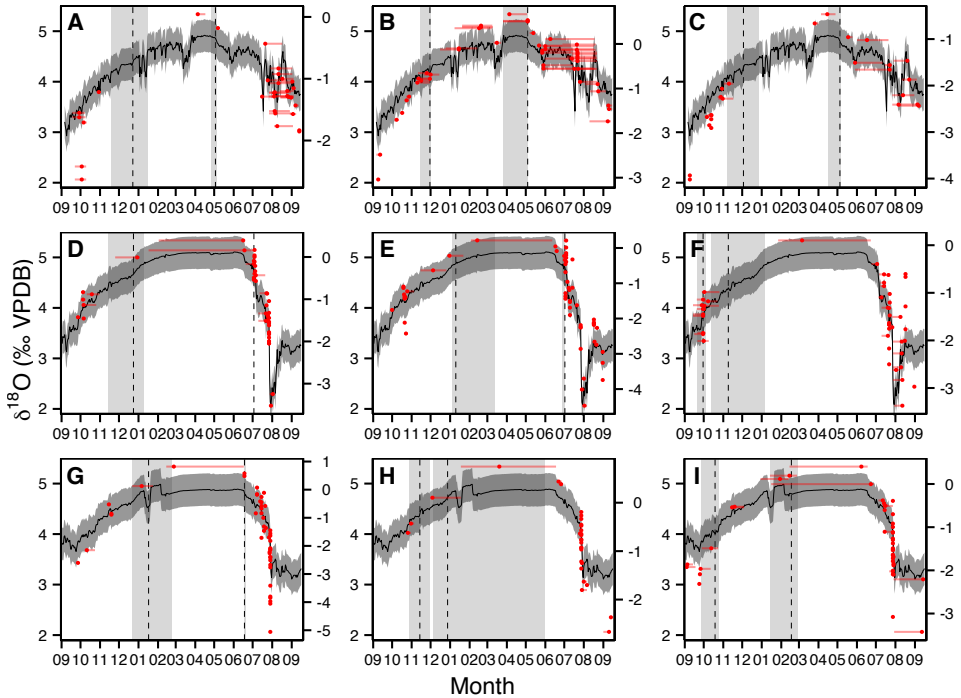
Figure 7. Dynamic time warping aligned measured SIMS δ^{18}O values. (**A**-**C**) specimens from the basket at 25 m depth in Kongsfjorden, (**D**-**F**) the basket at 15 m depth in Rijpfjorden, and the (**G**-**I**) basket at 25 m depth in Rijpfjorden. Specimens C, F, and I are *C. ciliatum*, and the rest are *S. groenlandicus*. Predicted δ^{18}O values are given as black line and follow the left Y-axis scale. Grey shading illustrates the 95% prediction interval for predicted δ^{18}O values. Red dots represent the DTW aligned dates for centroids of measured δ^{18}O values and follow the right Y-axis scale. Horizontal error bars indicate the maximum and minimum date assigned for each measured δ^{18}O value after 500 DTW permutations. Vertical dashed lines from the left indicate the DTW aligned beginning and end of the dark winter growth band, respectively. Grey shading under the dashed lines indicate the minimum and maximum dates assigned for the winter growth band during 500 DTW permutations.

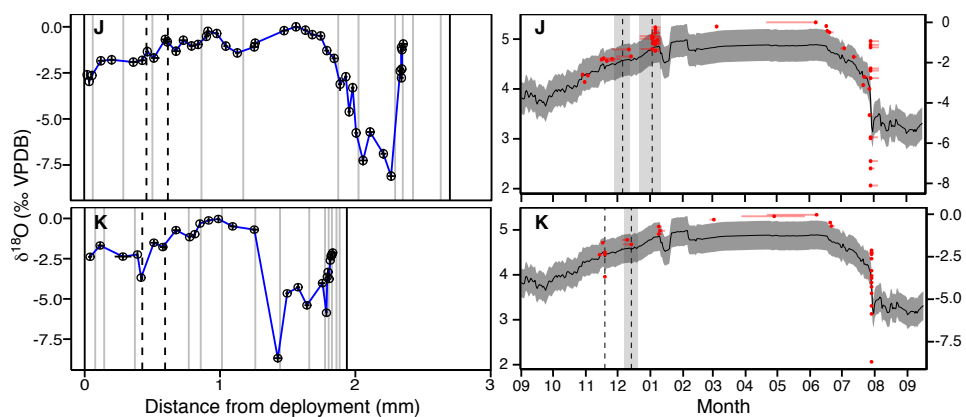**Figure 8. Samples with nomalously low δ^{18}O values**. Measured SIMS δ^{18}O values (left panels) and dynamic time warping aligned measured SIMS δ^{18}O values (right panels) for two *C. ciliatum* specimens (**J**, and **K**) with anomalously low δ^{18}O values towards the end of the shell growth from the basket at 25 m depth in Rijpfjorden. See Figures 6 and 7 for further explanation.
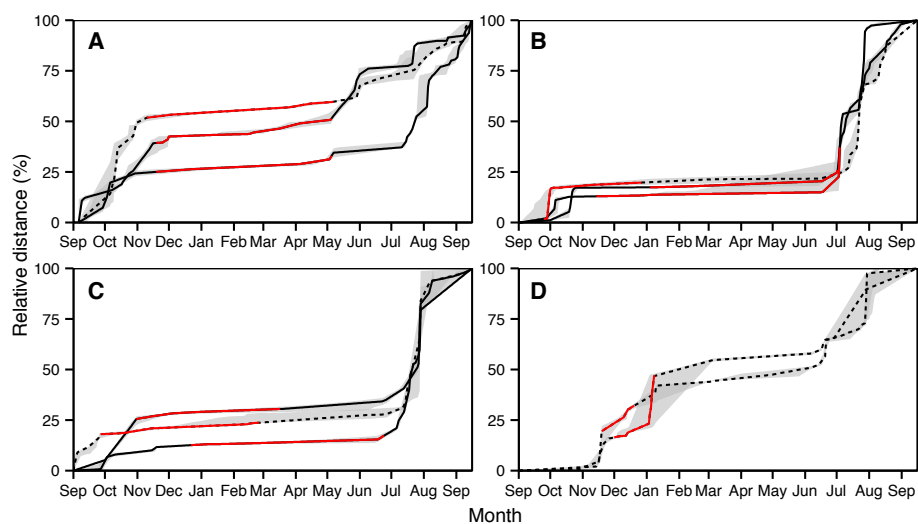
Figure 9. Growth models after matching δ^{18}O **values. A)** Kongsfjorden 25 m basket, **B)** Rijpfjorden 15 m basket, **C)** samples from Rijpfjorden 25 m basket with a decent DTW alignment fit, and **D)** samples from Rijpfjorden 25 m basket with anomalously low δ^{18}O values towards the end of the shell growth. Solid lines represent estimated growth models using centroids of SIMS samples for *S. groenlandicus* and dashed lines for *C. ciliatum*. Grey shading illustrates 2.5 and 97.5 % quantiles of 500 permutation runs. Red line illustrates the estimated maximum extent of winter growth band using quantiles.
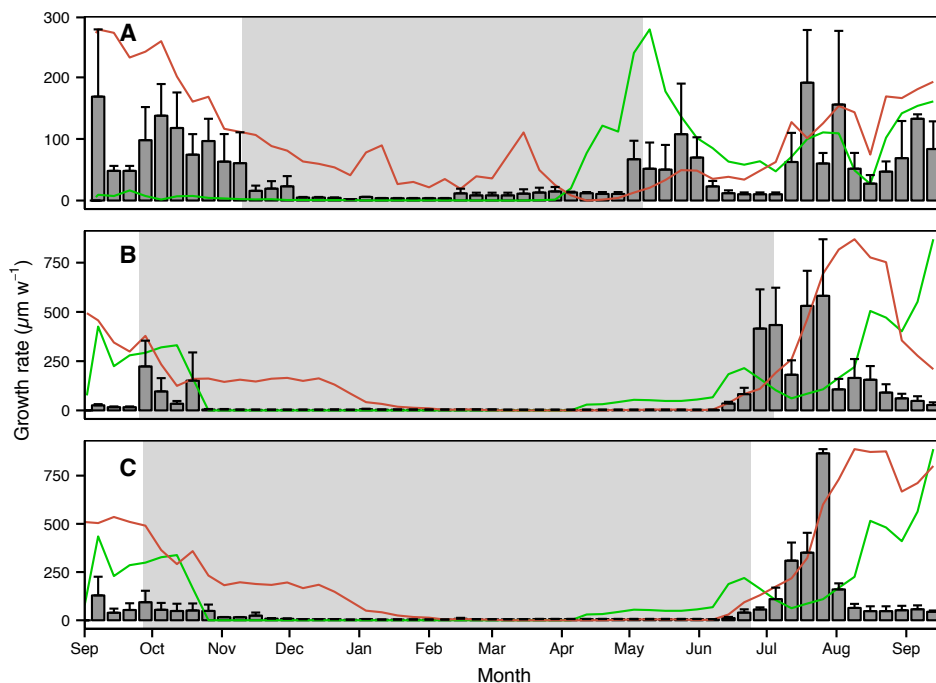
Figure 10. Shell growth rate related to mooring instrument data. Weekly averaged growth rate (gray bars) + 1 standard error (error bars) related to weekly averages of fluorescence index (green line) and temperature (red line). **A)** Kongsfjorden 25 m basket, **B)** Rijpfjorden 15 m basket, and **C)** Rijpfjorden 25 m basket. Fluorescence and temperature values are scaled to growth rate. Fluorescence measurements are from 36 m in Kongsfjorden and from 10 m in Rijpfjorden. The gray shaded area represents the estimated maximum extent for winter growth bands.

Tables

Table 1. Overview of analyzed bivalve shells and mooring instruments. Columns
from the left: the fjord; abbreviation used in figures (Abbr.); depth of bivalve baskets (Depth);
depth of mooring instruments (CTD) for salinity (S) and fluorescence (F) measurements;
number of $\delta^{18}O$ analyzed bivalves (n) per species (Ser = *S. groenlandicus*, Cil = *C. ciliatum*);
average shell height of bivalve species ($\pm$1SD); and deployment (In) and recovery dates (Out).
Temperature was measured using loggers attached to each basket.

Fjord	Abbr.	Depth (m)	CTD (m) S	F	n Ser	Cil	Height (mm) Ser	Cil	Deployment In	Out
Kongsfjorden	KB	25	36	36	3	1	30.2 ± 4.0	20.7	2009-09-05	2010-09-16
Rijpfjorden	RA	15	10	10	2	1	13.0 ± 1.8	16.3	2009-08-31	2010-09-19
Rijpfjorden	RB	25	26	-	2	3	25.9 ± 13.1	23.0 ± 2.6	2009-08-31	2010-09-19

Table 2. Goodness-of-fit indicators for aligned $\delta^{18}O$ profiles: Regression parameters
between predicted and measured $\delta^{18}O$ values (β_0 = intercept, β_1 = slope, R^2 = coefficient of
determination. P was < 0.001 for all regressions); Minimum, median and maximum measured
SIMS $\delta^{18}O$ value for each sample; Number of SIMS sample spots (N); Average offset $\pm$ SE (‰
VPDB) between measured and predicted $\delta^{18}O$ values (Offset); and average accuracy estimate for
aligned measured SIMS $\delta^{18}O \pm$ SE in days (Accuracy).

Sample	Basket	Species	Regression β_0	β_1	R^2	Measured SIMS $\delta^{18}O$ Min	Med	Max	N	Offset	Accuracy
A	KB	Ser	4.74	0.61	0.86	-2.63	-1.29	0.04	31	-5.25 ± 0.05	20 ± 2
B	KB	Ser	4.55	0.53	0.95	-3.04	-0.33	0.67	47	-4.79 ± 0.05	35 ± 3
C	KB	Cil	5.19	0.56	0.99	-4.02	-2.24	-0.47	25	-6.13 ± 0.08	17 ± 3
D	RA	Ser	4.79	0.70	0.92	-3.52	-1.14	0.39	45	-5.11 ± 0.05	11 ± 5
E	RA	Ser	4.94	0.59	0.87	-4.47	-1.41	0.21	58	-5.56 ± 0.07	6 ± 2
F	RA	Cil	4.49	0.52	0.56	-3.37	-1.48	0.10	45	-5.23 ± 0.07	11 ± 3
G	RB	Ser	4.54	0.23	0.74	-5.06	-1.46	0.82	47	-5.73 ± 0.15	4 ± 3
H	RB	Ser	4.41	0.47	0.86	-2.67	-0.67	0.75	29	-4.83 ± 0.08	9 ± 5
I	RB	Cil	4.61	0.37	0.74	-3.42	-1.49	0.40	44	-5.44 ± 0.08	15 ± 5
J	RB	Cil	4.75	0.16	0.53	-8.10	-1.38	0.00	44	-6.52 ± 0.25	8 ± 1
K	RB	Cil	4.71	0.18	0.56	-8.68	-2.28	-0.03	29	-6.85 ± 0.30	6 ± 3

Table 3. Linear mixed effect regression parameters between logarithm of growth rate and temperature (T), fluorescence index (F), and salinity (S). Individual shells and weeks from deployment were used as random effects. Treatment represents different baskets (see Table 1), "All" expressing the overall model for all data. Parameter refers to the model parameter (T, S, F = fixed effect, and β_0 = intercept). R^2_m gives the marginal coefficient of determination (variation explained by the fixed effect), whereas R^2_c indicates the conditional coefficient of determination (variation explained by the fixed effect as well as by the random effects). Estimate indicates estimated standardized intercept for β_0 and slope for T, F, and S. Remaining columns represent t-statistics estimated based on Satterthwaite's approximation for denominator degrees of freedom: standard error (SE), the approximate denominator degrees of freedom (DF), t-statistics (t-value) and the associated p-value from a t-distribution (p-value). R^2 values were calculated using Model 1, whereas the ANOVA statistics were estimated using standardized predictor variables and Model 2 (see Text S2 for details).

Treatment	Parameter	R^2_m	R^2_c	Estimate	SE	DF	t-value	p-value
KB	β_0			0.41	0.2	3.1	2.2	0.110
	T	0.30	0.48	0.93	0.1	66.8	10.0	**<0.001**
	F	0.11	0.47	0.48	0.1	49.1	6.7	**<0.001**
	S	0.01	0.48	0.14	0.2	55.0	0.6	0.538
RA	β_0			0.37	0.2	19.9	2.0	0.059
	T	0.39	0.71	0.85	0.3	57.0	3.3	**0.002**
	F	0.25	0.69	0.48	0.2	55.7	2.0	0.055
	S	0.27	0.70	-0.09	0.2	55.8	-0.5	0.590
RB	β_0			0.73	0.1	50.0	4.9	**<0.001**
	T	0.40	0.72	0.92	0.2	50.0	4.0	**<0.001**
	F	0.21	0.72	-0.21	0.2	50.0	-0.9	0.374
	S	0.27	0.72	-0.27	0.3	50.0	-0.8	0.404
all	β_0			0.55	0.1	27.6	4.4	**<0.001**
	T	0.29	0.53	0.74	0.1	240.4	8.7	**<0.001**
	F	0.07	0.53	0.34	0.1	402.7	4.6	**<0.001**
	S	0.03	0.53	-0.08	0.1	399.8	-1.1	0.262

Supporting Information Legends

Text S1. Alignment of predicted and measured intra-shell δ^{18}O profiles. Detailed information about dynamic time warping (DTW) procedure used to align SIMS-measured δ^{18}O profiles with predicted δ^{18}O profiles.

Text S2. Linear mixed model formulations used to examine the relationships between shell growth rate and mooring instrument recordings.

Data S1. Example dataset for DTW alignment presented in Text S1. The dataset is in R format (.rda) and can be opened in R using the *load()* function.

Data S2. SIMS δ^{18}O data. The file is in Excel format (.xlsx). Analyzed SIMS samples from bivalve shells are separated to "Shell_samples" tab, whereas Brown Yule Marble standards are presented in "BYM_standards" tab. See "Information" tab for column explanations.

Code S1. R scripts presented in Text S1. The file is in R script format (.R) and can be opened using R.

Code S2. R functions used in Code S1 and Text S1. The file is in R script format (.R) and can be opened using R.

Text S1: Alignment of predicted and measured intra-shell δ^{18}O profiles

SI1.1 Alignment example

Subannual growth patterns of *Serripes groenlandicus* and *Ciliatocardium ciliatum* were determined by aligning *in situ* SIMS-measured δ^{18}O profiles with predicted δ^{18}O profiles, the latter derived by combining continuous mooring seawater temperature and salinity records with a salinity–δ^{18}O relationship (see Material and Methods). One key aim of the alignment procedure was to establish a reproducible method, which would facilitate objective, rather than subjective, alignment of δ^{18}O profiles. Establishing such a method was, however, challenging due to signal noise in the measured SIMS δ^{18}O profiles and an offset between measured and predicted values. The signal noise and offset were likely caused by the surface (*in situ*) δ^{18}O measurement technique used in this study (see Discussion). The explanation here describes how the alignment method was chosen and applied using a subset of the data as a worked example. This example consists of data for the sample named "E" (*S. groenlandicus* specimen from the basket at 15 m depth deployed in Rijpfjorden; Table 2 in the main article). Data analyses were implemented using R statistical programming environment [1]. R scripts and data to reproduce all plots presented here are included as Supplementary Material. Example data is included as Data S1, the R script as Code S1, and the functions needed to run the script as Code S2. These functions are used to make the example code shorter and easier to read, but since the source code is available the functions can be freely modified. R packages *dtw* [2], *ggplot2* [3], *gridExtra* [4], *plyr* [5], and *scales* [6] have to be installed for the example scripts to work.

Dynamic time warping (DTW) was used to align the predicted and measured SIMS δ^{18}O profiles [2,7]. The DTW method consists of algorithms that were developed to align and compare temporal sequences, which might vary in time or speed (i.e. along the x-axis) [2,8–10], and was therefore a suitable method to achieve the alignment required by this study. In DTW the alignment of reference (predicted δ^{18}O values in this study) and query (measured SIMS δ^{18}O profiles) indexes are constrained by algorithms referred as "step patterns" [2,7]. A step pattern was chosen to allow the query index to be aligned along the reference index as flexibly as possible. The chosen step pattern, *symmetric2*, constrains the alignment by giving one diagonal step the same cost as two equivalent steps along the sides (see Figure 3 in Giorgino [2]). It allows assignment of one query index value to several reference index values, but also aligns several query index values to one reference index value.

SI1.2   Patterns in measured and predicted δ^{18}O profiles

Depending on the position along graphs' x-axes, predicted δ^{18}O values were 1 to 6 ‰ (all δ^{18}O values in this document are reported relative to VPDB) higher compared to measured SIMS values (Figure S1). In order to align the two δ^{18}O profiles it was necessary to assume that the measured SIMS δ^{18}O values along the shell section were consistently related to predicted δ^{18}O values within some random error (signal noise). In other words, the relationship between a predicted and measured value was assumed to be:

$$\delta^{18}O_{predicted} = \beta_1 \; \delta^{18}O_{measured} + \beta_0 + \epsilon \tag{S1}$$

where β_1 and β_0 are the slope and intercept of the linear regression between all predicted and measured SIMS δ^{18}O values within a shell sample (see Table 2), and ϵ is the random error or noise in the measured δ^{18}O signal for each SIMS measurement separately (analogous to residuals). It should be noted that the noise component does not necessarily indicate biased δ^{18}O measurements, but is simply assigned to measured values which do not fit the resulting DTW alignment model.

The predicted δ^{18}O profile for the worked example was characterized by lower values at the beginning of the deployment (September 2009 until January 2010) and again late during the deployment (July 2010 until recovery, Figure S1). Measured SIMS δ^{18}O values were low until approximately 600 μm from calcein mark indicating that this part of the shell was deposited relatively soon after deployment. After this δ^{18}O values demonstrated a large increase over a short distance (600 - 640 μm), possibly indicating cessation, or slowing down, of shell growth. After reaching maximum at 640 μm, measured SIMS δ^{18}O values fluctuated between -1.44 and 0.21 ‰ until a gradual decline that started after 1500 μm. The cause for the fluctuation is unknown. Nevertheless, judging from two other samples from the same basket deployed in the basket at 15 m depth within Rijpfjorden (Figure 6 in the main article), where similar fluctuation after the growth line was not present, this fluctuation could be assigned to noise component (ϵ) in the measured δ^{18}O signal. After reaching a minimum at 2870 μm measured SIMS δ^{18}O values increased again – a pattern that mirrored well the predicted δ^{18}O values from August until recovery in mid-September.

Identifying the position along the shell section where measured SIMS δ^{18}O values started to decrease ties that shell distance to mid-June 2010 coinciding with a sharp decline in predicted shell δ^{18}O values. Due to the SIMS-measured δ^{18}O fluctuation between 640 and 1500 μm there were two feasible scenarios: 1) Measured SIMS δ^{18}O values would start decreasing at 1500 μm. Values between 1000 and 1200 would contain large amount of negative signal noise ($-\epsilon$). 2) Measured values would start decreasing after 640 μm. Values between 1200 and 1500 would contain some positive signal noise, and values between 1000 and 1200 would be associated with some negative signal noise. The first scenario is supported by specimen D, where measured SIMS δ^{18}O values remain high until the middle of the shell section ($\sim$ 2000 μm from calcein line, Figure 6). On the other hand, the second scenario is supported by specimen F (*C. ciliatum* from basket at 15 m depth in Rijpfjorden), where measured SIMS δ^{18}O values begin to decline right after the measured δ^{18}O maximum at distance of 664 μm, only one fifth of the distance from the shell margin (Figure 6). Replicate samples, therefore, do not shed more light into the problem at hand and it is necessary to acknowledge that both scenarios are equally valid by purely looking

855
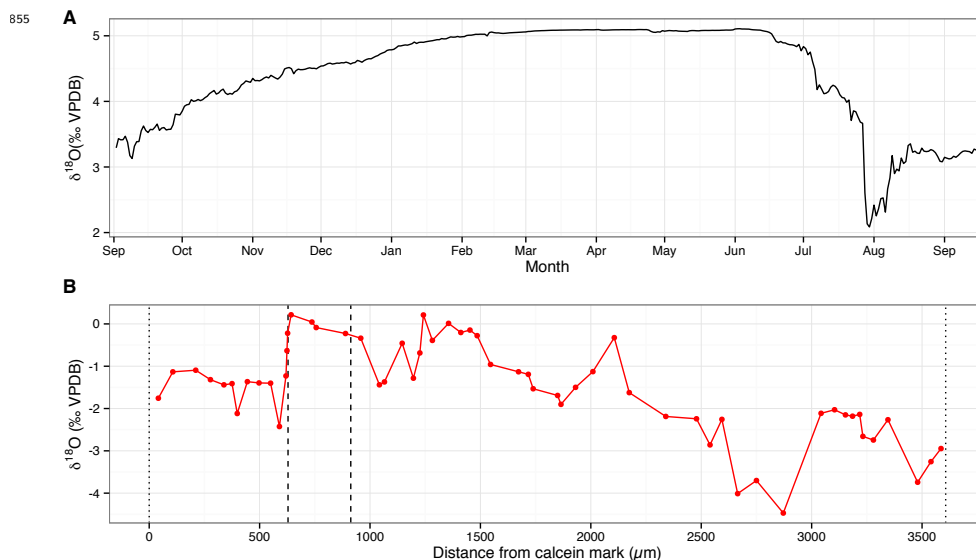

Figure S1. A) Predicted aragonite bivalve shell $\delta^{18}O$ values at 10 m depth in Rijpfjorden. X-axis represents time through the deployment period ticks specifying the first day of each month. **B)** *In situ* measured SIMS $\delta^{18}O$ values for specimen E (*Serripes* specimen from basket at 15 m depth in Rijpfjorden; Table 2). Dashed vertical lines indicate the beginning and the end of the dark winter growth band. Dotted vertical lines represent the calcein line that denotes the start of the field deployment and the margin of the shell section, on the left and right respectively. X-axis represents distance in μm measured from deployment, i.e. the calcein line.

74 at the worked example data.

SI1.3 Standardization of measured SIMS $\delta^{18}O$ profiles and the initial DTW

76 Due to the offset between measured SIMS and predicted $\delta^{18}O$ values, the measured $\delta^{18}O$ profile
77 was standardized to the minimum and maximum of predicted $\delta^{18}O$ profiles before running the
78 DTW alignments. The chosen standardization procedure resulted in maximum measured SIMS
79 $\delta^{18}O$ values being aligned with maximum predicted $\delta^{18}O$ values and enhanced the assignment
80 of non-fitting values as noise component (ϵ) in measured signal following the first assumption
81 (Equation S1). Further, the procedure also lead to an assumption that maximum and minimum
82 $\delta^{18}O$ values were measured along each shell section. The bias introduced by this assumption,
83 however, was evaluated small as the resulting DTW alignments were primarily driven by the
84 period of decrease in measured SIMS $\delta^{18}O$ values aligned with the rapid decline in predicted
85 $\delta^{18}O$ values from July to August (Figure S1).

An initial DTW alignment was run using the standardized measured SIMS δ^{18}O values as query index and the predicted δ^{18}O values as the reference index (Figure S2A). The model resulted in an alignment following scenario 1, as explained in the previous section. Fluctuation in measured SIMS δ^{18}O values between 640 and 1200 μm was interpreted as negative signal noise $(-\epsilon)$ as demonstrated by eight query index values being assigned to one day in mid-February (Figure S2A). Consequently, the resulting growth model indicated approximately 600 μm of shell growth for the same day in mid-February (Figure S2B). Sudden shell growth in mid winter is not likely in a high Arctic fjord with an extreme seasonality and food source returning at the earliest in April-May in the form of ice algae [11–13]. This initial DTW alignment performed poorly with several non-fitting values, including at the both ends of the reference index. Therefore, the DTW alignment had to be improved.
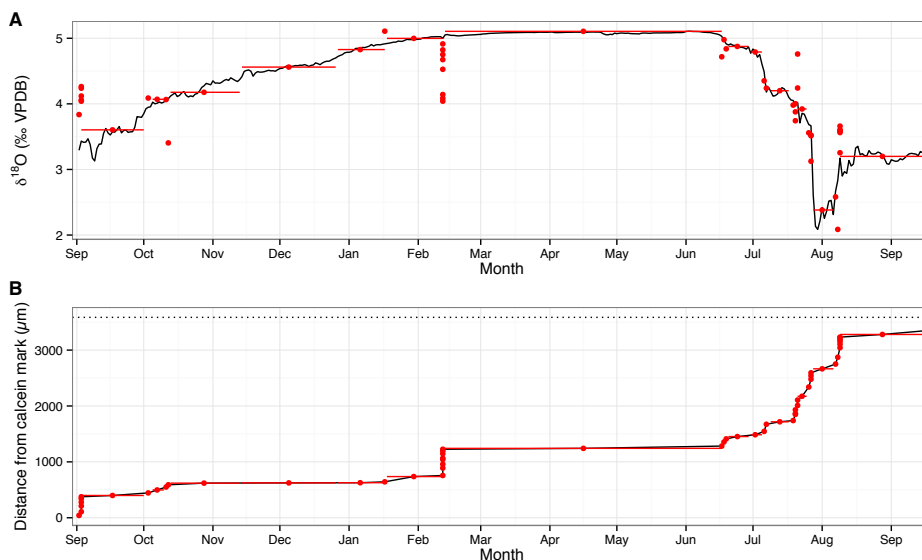

Figure S2. A) Initial DTW output that aligned standardized measured SIMS δ^{18}O values (red dots, query index) overlaid with the predicted δ^{18}O values (black line, reference index). Horizontal error bars indicate query index values that were assigned to several reference index values, thereby giving the minimum and maximum date for each query index value. Red dots on top of each other represent instances where several query index values were assigned to single reference index value, suggesting that these measured values became modeled as signal noise (ϵ). **B)** Resulting sub-annual bivalve shell growth model (black line). Horizontal dotted line indicates the shell margin. Red dots and horizontal error bars are as described in **A**.

SI1.4 Addition of margins

The placing of early and late query index values can be improved by encouraging the DTW algorithm to do an open-ended alignment [2]. Since the predicted δ^{18}O values for the deployment calcein mark (dist $= 0$ μm) and shell margin (dist $= 3607$ μm) had been estimated, the predicted δ^{18}O values of the first and last day of mooring deployment were added as standardized δ^{18}O values for the beginning and the end of the measured SIMS profile (query index). In the resulting second DTW alignment, the non-fitting values at the beginning and end of the measured SIMS δ^{18}O profile were moved to mid-September and early-August respectively (Figure S3). Lower measured SIMS δ^{18}O values between 640 and 1200 μm were still assigned to one day in mid-February suggesting a higher growth rate that time. As stated in the previous section, such growth is not believable and the DTW alignment required further improvements.

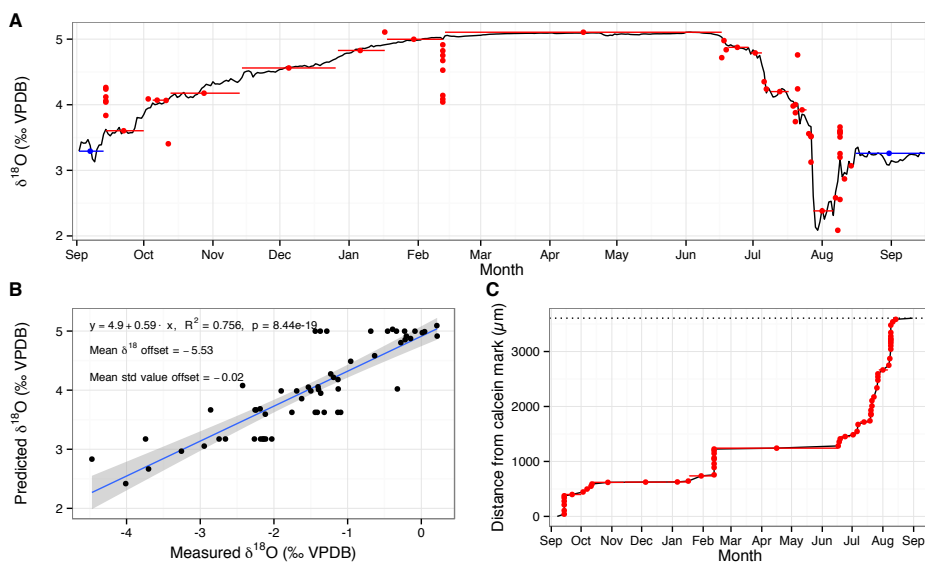**Figure S3. A)** Second DTW alignment of standardized measured SIMS δ^{18}O values (red dots) overlaid with predicted δ^{18}O values (black line), after inclusion of the first and last predicted value (blue dots). See Figure S2 for detailed explanation. **B)** Resulting regression relating predicted δ^{18}O values as a function of measured SIMS δ^{18}O values (Equation S1). Blue line indicates the regression model and grey shading the 95 % confidence intervals for the model. **C)** Resulting subannual growth model (black line). Horizontal dotted line indicates the shell margin. Red dots and horizontal error bars are as described in **A**, except that the first and last predicted δ^{18}O values are removed from the plot.

SI1.5 Matching the query index length with the reference index length

In the previous DTW runs, the alignment procedure did not consider the distance between measured SIMS δ^{18}O samples (X-axis in Figure S1B), because the query index was represented as a sequence of 60 values (58 SIMS δ^{18}O measurements and margins), which were then aligned with 380 daily values of predicted δ^{18}O. Further, DTW algorithms might not always perform optimally in cases when the length of query and reference indexes differ drastically [14]. Consequently, it was possible to improve the DTW alignment by making the indexes the same length and simultaneously adding some of the distance information to the query index (measured SIMS δ^{18}O profile). This was done by upsampling the query index (measured SIMS δ^{18}O values) using linear interpolation and a constant distance along the distance axis for measured SIMS δ^{18}O values (Figure S1B). Since this study was also attempting to estimate the timing for the winter growth band (Figure 7 in the main article; see also [12]), intra-shell growth lines were first added as distances for linear interpolation and then complimented with additional points using a constant interval such that the length of query index (measured SIMS δ^{18}O values) matched with the length of the reference index (predicted daily δ^{18}O values).

The resulting third DTW alignment generally demonstrated a much better fit compared to the two previous models (Figures S4A-B, S3A-B and S2A). Two measurements at 398 and 589 μm were assigned to late October and associated with large amount of negative noise ($-\epsilon$, Figure S4A). This alignment is believable since both SIMS measurements had lower δ^{18}O values compared to proximal values (Figure S1A). Furthermore, 10 measured SIMS δ^{18}O values were all assigned to late October, which would mean approximately 500 μm of shell growth within a couple of days (Figure S4C). Although the magnitude of the growth rate is likely an overestimate, the general timing for this growth is feasible: Leu *et al.* [11] reported 28% of maximum chlorophyll-a concentration in pelagic particular organic matter measured in Rijpfjorden in 2007-2008 to take place in October indicating that bivalves would still have get enough nutrition to sustain shell growth during the autumn (September to November). The resultant subannual growth model estimated a growth cessation to last from November until mid-June (Figure S4C). Due to the 10 values assigned within couple of days in late October, the timing for the beginning of the growth hiatus is associated with a low confidence, but the general subannual shell growth pattern seems feasible since the mooring fluorescence data indicated the return of an algal food source in mid-June (Figure 5). The winter growth band coincides with the growth cessation which is estimated to have commenced in January and to have ended in July. Due to almost invariant predicted δ^{18}O values, the beginning of the winter growth band cannot be estimated accurately, as it could take place any time between January and June. The end of the winter growth band, on the other hand, is coincident with decreasing predicted δ^{18}O values and consequently is a relatively robust estimation within the model framework. The non-fitting measured SIMS δ^{18}O values in earlier models were now assigned to early July (Figure S4A). Although many of these values were still associated with one reference index value, they varied on both sides of the predicted values (both negative and positive residuals) increasing the fit of the regression model ($R^2 = 0.87$ as opposed to 0.76 of the second DTW alignment). Hence, it is possible to conclude that the alignment, which follows the scenario 2 introduced in Section SI1.2, does perform relatively well with these data, although the resulting growth rates caused by assignment of multiple measured SIMS δ^{18}O values to one day are likely overestimates. Another drawback

859

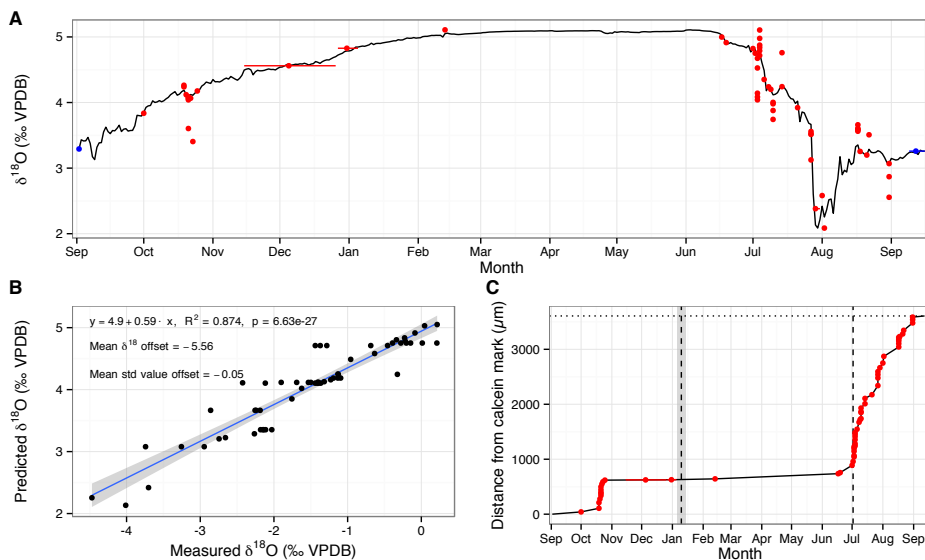**Figure S4. A)** Third DTW alignment after linear interpolation of measured SIMS δ^{18}O values. See Figure S2A and text for detailed explanation. **B)** Resulting regression relating predicted δ^{18}O values as a function of measured SIMS δ^{18}O values. See Figure S3B for detailed explanation. **C)** Resulting sub-annual growth model. The plot is the same as Figure S3C, but the beginning and end of the winter band are now added as dashed vertical lines. Grey shading represents the estimated minimum and maximum date for each line.
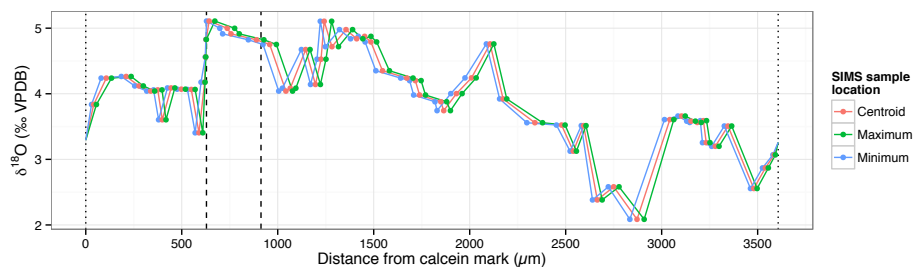

Figure S5. Linear interpolation for centroid, maximum and minimum distance point of each SIMS sample spot.

with this DTW model is that it does not assign enough uncertainty to assigned values as by eye one can see that some measured $\delta^{18}O$ values could be easily moved by several months without changing the fit dramatically (the one assigned to late February in Figure S4A, for instance).
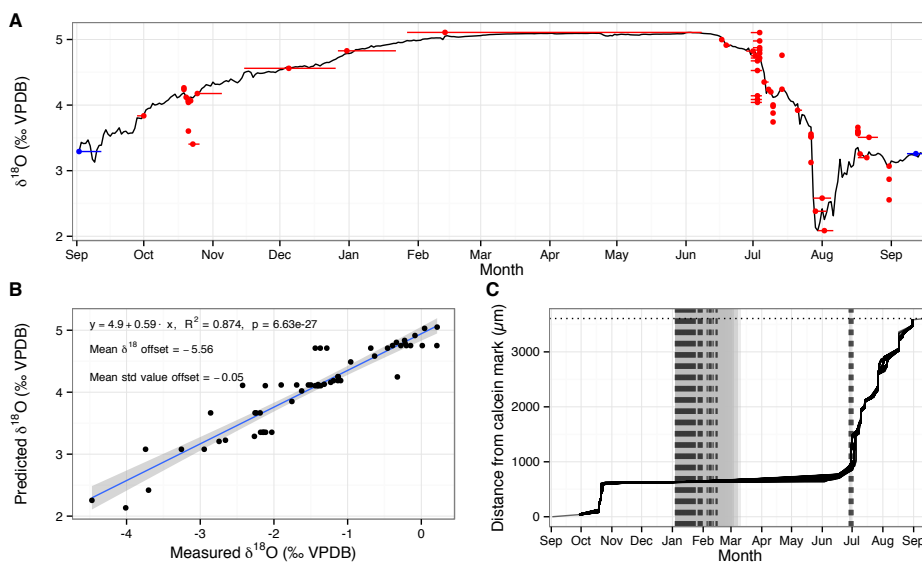

Figure S6. A) Permuted DTW alignment using linear interpolation and *symmetric2* step pattern. Red dots indicate the assigned date for centroids of SIMS sample spots. Horizontal error bars represent the minimum and maximum date encountered during 500 DTW runs using randomly sampled distance values within the minimum and maximum extent of SIMS sample spots. Blue dots with error bars indicate the alignment of added deployment and recovery predicted $\delta^{18}O$ values. **B)** Resulting regression fit for the centroids. Identical to non-permuted DTW (Figure S4B). **C)** Subannual growth model for 500 permutation runs. Each black line is transparent and indicates a separate DTW run. Dashed vertical lines are also transparent and indicate the estimated average date for the beginning and the end of the winter growth band for each DTW run.

SI1.6 Estimating the uncertainty for aligned measured SIMS $\delta^{18}O$ values

The third DTW modeling approach has been shown to result in feasible subannual growth model. Consequently, it is possible to proceed to estimation of the uncertainty of aligned query index values. Even though the SIMS sampling spot diameter was only 20.0 μm on average, sampled shell material was likely significantly time-averaged wherever shell growth rate was low (Figure S5, [15,16]). The maximum and minimum extent of each SIMS sample spot was used to randomly

sample distance values between these limits for each measured SIMS δ^{18}O value. The resulting permutation not only changes the distance of each measured SIMS δ^{18}O value, but might also change the order, if maximum and minimum limits of adjacent samples overlapped (Figure S5). A new DTW alignment model was calculated by repeating the permutation a sufficient number of times (n = 500). The DTW model demonstrated an increased uncertainty for measured δ^{18}O value alignment (Figure S6). The vertical error bars covered almost the entire extent where a measured value could be placed by eye.

The final DTW alignment estimated a mean offset between predicted and measured δ^{18}O values as -5.56 ‰, and provided a significant regression between the predicted and measured δ^{18}O values with an R^2 of 0.87 (Figure S6B). The offset of -0.05 ‰ in standardized values demonstrated a relatively good average fit. Estimated regression parameters (β_0 and β_1) were used to calculate the signal error term (= residuals, ϵ) for each measured value. The error term ranged between -0.50 and 0.62 ‰ with two values < -0.4 ‰, four values between 0.4 and 0.6 ‰ and two values > 0.6 ‰. Ten measured standardized δ^{18}O values were 10–20 % lower, five values 10–20 % higher and two values 20–30 % higher compared to predicted values. Deposition of the winter growth band was estimated to begin sometime between January and March and end in July. The general subannual growth pattern was almost identical to the third DTW alignment (Figure S4) with most of the annual growth occurring from July until recovery in mid-September.

References

1. R Core Team (2014). R: A language and environment for statistical computing. R Foundation for Statistical Computing, Vienna, Austria. URL `http://www.r-project.org`.

2. Giorgino T (2009) Computing and visualizing dynamic time warping alignments in R : the dtw package. J Stat Softw 31: 1–24.

3. Wickham H (2009) ggplot2: elegant graphics for data analysis. New York, NY, USA: Springer, 1st edition, 1–211 pp. URL `http://had.co.nz/ggplot2/book`.

4. Auguie B (2012). gridExtra: functions in Grid graphics. URL `http://cran.r-project.org/package=gridExtra`.

5. Wickham H (2011) The Split-Apply-Combine Strategy for Data Analysis. J Stat Softw 40: 1–29.

6. Wickham H (2014). scales: Scale functions for graphics. URL `http://cran.r-project.org/package=scales`.

7. Müller M (2007) Dynamic time warping. In: Information Retrieval for Music and Motion, Berlin / Heidelberg, Germany: Springer, chapter 4. pp. 69–84.

8. Sakoe H, Chiba S (1978) Dynamic programming algorithm optimization for spoken word recognition. IEEE Trans Acoust 26: 43–49.

9. Senin P (2008) Dynamic time warping algorithm review. Technical report, Information and Computer Science Department, University of Hawaii, Honolulu, USA.

10. Hladil J, Vondra M, Cejchan P (2010) The dynamic time-warping approach to comparison of magnetic-susceptibility logs and application to Lower Devonian calciturbidites (Prague Synform, Bohemian Massif). Geol Belgica 13: 385–406.

11. Leu E, Søreide J, Hessen D, Falk-Petersen S, Berge J (2011) Consequences of changing sea-ice cover for primary and secondary producers in the European Arctic shelf seas: Timing, quantity, and quality. Prog Oceanogr 90: 18–32.

12. Ambrose Jr WG, Renaud PE, Locke V WL, Cottier FR, Berge J, et al. (2012) Growth line deposition and variability in growth of two circumpolar bivalves (*Serripes groenlandicus*, and *Clinocardium ciliatum*). Polar Biol 35: 345–354.

13. Daase M, Falk-Petersen S, Varpe O, Darnis G, Søreide JE, et al. (2013) Timing of reproductive events in the marine copepod *Calanus glacialis*: a pan-Arctic perspective. Can J Fish Aquat Sci 70: 871–884.

14. Ratanamahatana CA, Keogh E (2005) Three myths about dynamic time warping data mining. In: Kargupta H, Srivastava J, Kamath C, Goodman A, editors, Proc 2005 SIAM Int Conf Data Min, Philadelphia, PA: Society for Industrial and Applied Mathematics. p. 5. doi:10.1137/1.9781611972757. URL http://epubs.siam.org/doi/book/10.1137/1.9781611972757.

15. Goodwin D, Flessa K, Tellezduarte M, Dettman D, Schöne BR, et al. (2004) Detecting time-averaging and spatial mixing using oxygen isotope variation: a case study. Palaeogeogr Palaeoclimatol Palaeoecol 205: 1–21.

16. Beelaerts V, Ridder F, Schmitz N, Bauwens M, Dehairs F, et al. (2008) On the elimination of bias averaging-errors in proxy records. Math Geosci 41: 129–144.

Text S2: Linear mixed model formulations used to examine the relationships between shell growth rate and mooring instrument recordings

Linear mixed models were calculated using lme4 package [1] for R [2].

Model 1

The first model was used to examine the variance explained by each response variable separately. The model was formulated using R notation:

$$lmer(log(GR) \sim X + (1|Smp) + (1|W), \ data = D) \tag{S1}$$

Where D is the data frame. GR represents a column of D containing information of weekly growth rate, X weekly averaged temperature, fluorescence index or salinity, Smp sample names of individual bivalve shell sample names as factor, W a vector of weeks from the deployment as numeric. S and W represent random effects. The notation $(1|S)$ specifies that random intercepts and constant slopes should be used for a random effect [1, 3]. The marginal and conditional R^2 were calculated from the $lmer()$ output (object called model1):

$$r.squaredGLMM(model1) \tag{S2}$$

Using MuMIn package [4] and the method described in Johnson [5].

Model 2

The second model was used to examine the relative effect of each fixed effect (temperature, fluorescence index, and salinity) on logarithm of growth rate. Fixed effects were first scaled to centered to their means and scaled to their standard deviations:

$$scale(D[c("T","F","S")]) \tag{S3}$$

Where D is the data frame, and T, F and S the columns containing temperature, fluorescence index and salinity information respectively. The model was calculated using the scaled dataset (Ds):

$$lmer(log(GR) \ T + F + S + (1|Smp) + (1|W), data = Ds) \tag{S4}$$

The significance of T, F and S was estimated by Satterthwaite approximation for denominator degrees of freedom [6] using lmerTest package [7]:

$$summary(model2) \tag{S5}$$

Where model2 is the output from S4.

References

1. Bates D, Maechler M, Bolker B, Walker S (2014). lme4: Linear mixed-effects models using Eigen and S4. R package version 1.1-7. URL http://cran.r-project.org/package=lme4.

2. R Core Team (2014). R: A language and environment for statistical computing. R Foundation for Statistical Computing, Vienna, Austria. URL http://www.r-project.org.

3. Baayen R, Davidson D, Bates D (2008) Mixed-effects modeling with crossed random effects for subjects and items. J Mem Lang 59: 390–412.

4. Barton K (2014). MuMIn: Multi-model inference. R package version 1.10.5. URL http://cran.r-project.org/package=MuMIn.

5. Johnson PC (2014) Extension of Nakagawa & Schielzeth's R^2_{GLMM} to random slopes models. Methods Ecol Evol 5: 944–946.

6. SAS Technical Report R-101 (1978) Tests of hypotheses in fixed-effects linear models. Technical report, SAS Institute Inc., Cary, NC, USA.

7. Kuznetsova A, Bruun Brockhoff P, Haubo Bojesen Christensen R (2014). lmerTest: Tests for random and fixed effects for linear mixed effect models (lmer objects of lme4 package). R package version 2.0-11. URL http://cran.r-project.org/package=lmerTest.